



UNIFIED APPLICATION OF VAPOR SCREEN FLOW VISUALIZATION AND PRESSURE SENSITIVE PAINT MEASUREMENT TECHNIQUES TO VORTEX- AND SHOCK WAVE-DOMINATED FLOW FIELDS

Gary E. Erickson
Gary.E.Erickson@nasa.gov
Configuration Aerodynamics Branch
NASA Langley Research Center
Hampton, Virginia 23681
USA

KEYWORDS:

Main subjects: *aircraft and missile aerodynamics, flow visualization*

Fluid: *air*

Visualization methods: *laser vapor screen, pressure sensitive paint*

Other keywords: *vortex flows, shock waves, subsonic, transonic, supersonic*

ABSTRACT: *Laser vapor screen (LVS) flow visualization and pressure sensitive paint (PSP) techniques were applied in a unified approach to wind tunnel testing of slender wing and missile configurations dominated by vortex flows and shock waves at subsonic, transonic, and supersonic speeds. The off-surface cross-flow patterns using the LVS technique were combined with global PSP surface static pressure mappings to characterize the leading-edge vortices and shock waves that coexist and interact at high angles of attack (α). The synthesis of LVS and PSP techniques was also effective in identifying the significant effects of passive surface porosity and the presence of vertical tail surfaces on the flow topologies. An overview is given of LVS and PSP applications in selected experiments on small-scale models of generic slender wing and missile configurations in the NASA Langley Research Center (NASA LaRC) Unitary Plan Wind Tunnel (UPWT) and 8-Foot Transonic Pressure Tunnel (8-Foot TPT).*

1 General Introduction

The understanding and control of leading-edge vortex flows, shock waves, mutual interactions of vortices and shock waves, and flow-field interactions with airframe components is a continuing challenge for designers of modern military and commercial aircraft and missile configurations. Wind tunnel testing is a primary means of visualizing and quantifying the aerodynamic characteristics of advanced aerospace vehicle configurations at subsonic, transonic, and supersonic speeds. A multitude of test techniques exist to examine the on-surface and off-surface flow field characteristics, many of which feature optical methods that are well-suited to reveal the complexities of vortex- and shock wave-dominated flow fields in the subsonic through supersonic speed regimes. The LVS flow visualization method [1] was used in selected experiments described in this paper to illuminate the cross-flow patterns about slender wing and missile models. The off-surface flow visualization results were combined with global surface static pressure response maps using the PSP technique [1].

Previous experience [2]-[4] indicates that the LVS and PSP techniques are complementary, since each technique affords new insights or corroborative findings regarding the physics of the vortex flows and shock waves that form on slender wing and slender body configurations. The application of the two techniques is mutually exclusive, however, because of competing light sources and locations for the LVS and PSP optical components, different model surface preparations, and wind tunnel test condition requirements. Consequently, the two techniques were applied in separate phases of the selected experiments, which required appropriate planning and efficient use of wind tunnel facility resources. Representative results obtained on three selected configurations in separate experiments are presented in this paper. One experiment was conducted in the NASA LaRC UPWT using a 65-degree cropped delta wing model with leading-edge extension (LEX) and centerline and twin, wing-mounted vertical tails. The LEX was tested with and without passive surface porosity for vortex control. Two experiments were performed in the NASA LaRC 8-Foot TPT using a double-delta wing model featuring a $76^\circ/40^\circ$ strake-wing planform and a faceted missile model with chine-like cross sections. Detailed discussions of the results obtained in the UPWT and 8-Foot TPT testing of the cropped delta wing-LEX, double delta wing, and faceted missile models are provided in [2], [3], and [4], respectively.

2 Flow Visualization and Measurement Techniques

2.1 Laser Vapor Screen

The vapor screen method of flow visualization has been used in wind tunnel testing for several decades to visualize vortices, vortex sheets, lines of flow separation and reattachment, and shock waves at subsonic, transonic, and supersonic speeds. Water is injected into the wind tunnel circuit in a controlled manner and in sufficient quantity to promote condensation of water vapor in the test section. A laser is often used to produce an intense sheet of light that is projected into the test section typically in a plane perpendicular to the longitudinal axis of the tunnel or to the body axis of the model. At supersonic speeds, the temperature drop from the expansion in the supersonic nozzle causes the water vapor to condense into a thin, uniformly-distributed fog. The distribution of condensed water vapor and, consequently, the amount of scattered light within the plane of the light sheet, is affected by the flow disturbances created by the model. This phenomenon permits the observation and documentation of vortex cross sections, for example, at high angles of attack. Condensation first appears in the free stream at supersonic speeds, so that vortex flows appear as dark regions in the absence of scattered light surrounded by a light background. The change in flow density through oblique shock waves results in a similar change in fog density so that shock positions and shapes are often clearly defined. Separated flows such as wakes, vortex feeding sheets, and vortex core regions appear as dark or transparent, since condensate does not appear to be convected across the shear lines. At subsonic and transonic speeds, the condensed water vapor generally appears near the central region of the vortices, so the vortex cross sections appear as light regions within a darker background. A combination of the two light-scattering patterns often occurs at transonic speeds. LVS results are considered qualitative, although relative positions, sizes, and shapes of vortices and shock waves can be extracted from the vapor screen images, as desired. The appearance of condensation in the test section will affect the free-stream flow characteristics and the quantitative measurements of the model surface pressures and forces and moments [1]. Condensation at supersonic speeds is accompanied by a stagnation pressure

loss and a decrease in the Mach number at the condensation shock [1]. Interpretations of the vapor screen images are still valid, however, and effective correlations can be made with the trends observed in quantitative model measurements such as surface static pressure distributions and six-component forces and moments. The LVS systems that were used in the NASA LaRC UPWT and 8-Foot TPT are described in [2]-[4]. The LVS images that are presented in this paper are digitized frames acquired from a personal computer video capture board connected to a miniature camera installed inside the test section on the model support system [1].

2.2 Pressure Sensitive Paint

PSP is a global optical surface static pressure measurement technique that is based on the oxygen-quenching characteristics of certain luminescent materials. The emitted light intensity varies inversely with the local oxygen partial pressure and, therefore, the air pressure, since oxygen is a fixed mole fraction of air. The key elements of a PSP system include photoluminescent material in the form of a paint applied to the test article, illumination source to excite the paint, imaging device such as a scientific-grade digital camera to document the paint in the excited state, and an image acquisition and processing system. An in-situ global calibration method was used in the NASA LaRC wind tunnels to calibrate the PSP. Specifically, pressure measurements were obtained at several discrete pressure tap locations on the model surfaces using an electronically-scanned pressure (ESP) measurement system, and the PSP intensity was calibrated from the pressure tap data at spatially corresponding locations. Every pixel in the painted portion of a PSP digital image is effectively a pressure tap, so the pressure distributions can be resolved to much greater detail in all applicable regions of the model. Similar to surface oil flow visualization, color-coded images depicting the calibrated PSP intensity field response (that is, the surface pressure response) provide pertinent information on the topology of the vortex flows and shock waves that induce the corresponding pressure distributions. The potential intrusive effects of the PSP on the aerodynamic characteristics can be controlled by minimizing the paint thickness and surface roughness. An assessment of PSP intrusiveness on the aerodynamic flow about selected models at subsonic through supersonic speeds is provided in [5]. The PSP systems used in the NASA LaRC UPWT and 8-Foot TPT are also described in [2]-[4].

3 Wind Tunnel Facilities and Test Conditions

3.1 NASA LaRC UPWT

The NASA LaRC UPWT is a continuous-flow, variable-pressure supersonic wind tunnel. The tunnel contains two test sections which are approximately 4 feet square and 7 feet long. Each test section encompasses only part of the Mach number (M) range of the tunnel. The nozzle ahead of each test section consists of an asymmetric sliding block which allows continuous Mach number variation during tunnel operation from 1.5 to 2.86 in the low Mach number test section and 2.3 to 4.63 in the high Mach number test section. A complete description of the facility is contained in [6].

The experiment using the 65-degree cropped delta wing-LEX model was performed in UPWT Test Section 1 at free-stream Mach numbers of 1.6 and 2.1, a Reynolds number of 2.0 million per foot, and a stagnation temperature of 120 degrees Fahrenheit (deg F). Optical access to the test section is through

a series of windows in the side walls. This required the model to be rolled to a wings-vertical position for the PSP phase of the experiment. Mechanical operation of the model support system in the yaw plane constrained the angle of attack to a maximum of approximately 8 degrees. The model was tested in the upright orientation for the LVS phase of the testing, which afforded an increased range of angle of attack using the standard pitch mechanism.

3.2 NASA LaRC 8-Foot TPT

The NASA LaRC 8-Foot TPT was designed for operation as a continuous-flow, closed-return, variable-pressure wind tunnel with control capability to independently vary Mach number, stagnation pressure, stagnation temperature, and humidity. The test section was square with corner fillets and a cross-sectional area approximately equivalent to that of an 8-foot diameter circle. The top and bottom walls of the test section were axially slotted to permit a continuous variation of the test section Mach number from 0.2 to 1.2. A detailed description of the 8-Foot TPT is provided in [7].

The testing of the double delta wing model was conducted at free-stream Mach numbers of 0.50, 0.85, and 1.20, a Reynolds number of 2.0 million per foot, and a stagnation temperature of 80 deg F. The testing of the faceted missile model was also performed in the 8-Foot TPT at free-stream Mach numbers of 0.90 and 1.20, a Reynolds number of 3.0 million per foot, and a stagnation temperature of 120 deg F. Optical access through a window positioned along the test section ceiling allowed testing of the models in the upright orientation for the LVS and PSP phases of the experiments. This provided the full range of angle of attack using the arc sector model support system.

4 Model Descriptions

4.1 Generic 65-Degree Cropped Delta Wing-LEX

A generic fighter model featuring a 65-degree cropped delta wing with sharp leading edges was used in the UPWT testing. The model was designed and fabricated for surface pressure and force and moment testing in subsonic, transonic, and supersonic wind tunnels. The wing had an NACA 64A005 airfoil section from the 40-percent chord station to the trailing edge. A sharp leading edge was obtained by fairing a biconvex circular-arc section into the NACA profile from the 40-percent chord station to the wing leading edge. The wing was mounted in a high position on a fuselage that served as a housing for balance and pressure instrumentation. The model was modified to include a wing LEX mounted to an integral strut or 'gooseneck,' a centerline vertical tail, and twin vertical tails on the wings. A flat-plate, 0.25-inch thick LEX having a 65°/90° planform and symmetrically-beveled leading edges was fabricated for this experiment. The exposed area of the LEX (left and right sides) was 15 percent of the reference wing area. The LEX incorporated a pattern of 0.05-inch diameter through-holes spaced 0.10-inch apart on center to provide a total porosity level of 14.75 percent relative to the LEX exposed area. The objective of this passive porosity concept was to control the strength of the LEX vortices and their interaction with the wing vortex flows for improved high angle-of-attack aerodynamics. The same LEX was tested with 0 percent porosity (solid LEX) by applying sealing tape having 1.8 mil thickness (0.0018 inches) along the lower surface to cover all of the through holes. The model with porous LEX, wing, and twin wing-mounted vertical tails is shown installed in UPWT Test Section 1 in fig. 1. A

photograph of the model rolled 90 degrees in preparation for PSP testing is also shown in fig. 1. Planview and sideview sketches of the wing, LEX, fuselage, and tails are provided in fig. 2. The right wing upper surface was instrumented with a total of 45 pressure orifices distributed in three spanwise rows. The pressure rows were located at 30 percent, 60 percent, and 80 percent of the distance, x , along the wing centerline chord, c , measured from the apex of the wing ($x/c = 0.30, 0.60$, and 0.80). The orifice nondimensional semispan location, y/s , is expressed in terms of the semispan distance, y , measured from the wing centerline divided by the wing local semispan, s . Consequently, y/s values of 0.0 and 1.0 correspond to the wing centerline and the right wing leading edge, respectively. The pressure orifices were connected to an internal ESP module with purge air capability, which allowed air to be routed through the orifices during the application of the PSP coating. This avoided having to mask off the pressure rows during the painting process.

4.2 Generic Double Delta Wing

The generic double delta wing model tested in the 8-Foot TPT was also designed and fabricated for surface pressure and force and moment testing in subsonic, transonic, and supersonic wind tunnel facilities. The 0.375-inch-thick wing featured a flat upper surface and sharp, beveled leading, side, and trailing edges. The leading-edge sweep angles of the highly-swept forward section, or strake, and the main wing panel were 76° and 40° , respectively. A fiberglass housing was attached to the lower surface of the wing and served as a protective cover for the ESP and balance instrumentation. Photographs of the double delta wing installed in the 8-Foot TPT test section are presented in fig. 3 and correspond to the unpainted model and the model with PSP coating applied. Both photographs show the model with modified strake-wing intersections, or fillets [3], which are not discussed in this paper. The planview and sideview sketches in fig. 4 show the dimensional details of the model. The model incorporated a total of 47 static pressure orifices distributed in three spanwise rows on the wing upper surface. The three rows were on the left-hand side of the wing at nondimensional axial positions of $x/c = 0.25, 0.75$, and 0.90 , which correspond, respectively, to 25 percent, 75 percent, and 90 percent of the distance, x , measured from the strake apex along the model centerline chord, c . The orifice nondimensional semispan location, y/s , is defined in the same manner as the 65-degree cropped delta wing model. Consequently, y/s values of 0.0 and -1.0 correspond to the wing centerline and the left wing leading edge, respectively. The pressure orifices were connected to a standard ESP module without purge air capability. Consequently, the pressure rows were masked off during the PSP coating application. These regions appear as unpainted strips in the processed PSP images.

4.3 Faceted Missile

The faceted missile model tested in the 8-Foot TPT was a 30-percent-scale slender lifting body representation of a proposed missile concept. The model was designed for the dual purpose of pressure and force and moment measurements, and it was compatible with testing in subsonic, transonic, and supersonic wind tunnels. The body was faceted and featured chine-like cross sections with sharp leading edges. Fig. 5 presents selected wind tunnel installation photographs of the missile model, which include the model unpainted and with PSP coating applied to the upper surface. Overall dimensions of the missile configuration are shown in fig. 6. The model top and side views and cross sections can generally be described as diamond shapes. The model had an expanding cross section forebody, a transitional region, and an aftbody with contracting cross section. The development of vortex flows from the sharp leading edges was expected. It was also anticipated that the flow field over

the model would exhibit asymmetries at sufficiently high angles of attack because of the slenderness of the model and the possible development of multiple vortices arising from the discontinuities in the model planform and changes in the cross-sectional shape along the length of the model. ESP pressures were measured at selected stations by full rings of orifices. In terms of the local semispan, pressure orifices were placed at the body centerline (0 percent semispan) and in 5-percent increments to 95 percent semispan. The model length was 36 inches, and the pressure rings were located at model stations (M.S.) 9.0, 20.50, 25.50, 30.00, and 34.50 inches. This arrangement provided one ring on the forebody (M.S. 9.00), one ring on the transition region (M.S. 20.40), and three rings on the aftbody (M.S. 25.50, 30.00, and 34.50). The pressure orifices were connected to standard ESP modules installed inside the model. Similar to the double delta wing model, the pressure rows were masked off during the application of the PSP coating, and the pressure rows appear as unpainted strips in the PSP images. The field-of-view that was selected for the PSP testing was the model upper surface and included the pressure measurement stations at M.S. 20.40, 25.50, and 30.00. The ESP measurements and LVS flow visualization results shown in this paper correspond to these model stations.

5 Discussion of Results

5.1 Generic 65-Degree Cropped Delta Wing-LEX

Fig. 7 presents PSP and LVS results obtained on the 65-degree cropped delta wing model with solid LEX and porous LEX at $M = 1.6$ and $\alpha = 8^\circ$. The false-colored PSP images at the top of fig. 7 show the wing upper surface pressure response. The LEX was unpainted and, therefore, is not visible in the PSP images, which have undergone registration, ratioing, and resection transform [1]. Image registration marks (small black circles) are visible in the PSP images. The model fastener holes were initially filled with automotive putty, and these holes are also visible as larger dark circles through the PSP coating. The holes were filled with dental plaster prior to repeat applications of the PSP, which eliminated the appearance of the fastener holes in the processed images. A color bar indicates that green, blue, and purple correspond to regions of progressively lower pressure (that is, higher suction pressures), with purple representing the highest suction pressure levels. Regions of higher surface pressure (lower suction pressures or slightly positive pressures) are represented by shades of yellow, red, and pink. The LVS images for each configuration are shown directly below the corresponding PSP image, and they depict the condensation patterns in cross sections at approximately 60 percent, 80 percent, and 100 percent of the distance along the wing centerline chord measured from the wing apex ($x/c = 0.60, 0.80$, and 1.00 , respectively). The three x/c stations are identified as red dashed lines in the PSP images, and the $x/c = 0.60$ and $x/c = 0.80$ stations are locations at which discrete spanwise surface static pressure measurements were acquired along the right wing upper surface using the ESP method. The $x/c = 1.00$ station is at the wing trailing edge. The left portion of the LVS image at $x/c = 1.00$ is in the shadow of the centerline tail, since the laser light sheet was projected into the test section through a window in the right-hand wall. The LVS images are scaled relative to each other to reflect the growth of the vortices from the forward to aft portions of the wing. The LVS images are also approximately scaled relative to the PSP images so that the vortex cross sections in the LVS images can be projected to the corresponding regions of higher suction pressures in the PSP images. Important features of the PSP and LVS images are identified with numbers, and a descriptive key is provided in the figure. The location of the LEX-wing junction is also denoted.

The PSP image obtained with the solid LEX in fig. 7 reveals subtle pressure signatures induced by the LEX vortices and denoted by narrow bands of dark green/light blue colors extending in a nearly streamwise direction along the wing. There is a region of higher pressures denoted by yellow, red, and pink along the forward region of the wing and between the LEX vortex pressure footprints. A dominant feature of the PSP image are the broader bands of blue and purple color extending inboard from the wing leading edges, which are associated with the wing vortical flows. The footprint of an oblique shock wave beginning near the apex of the centerline tail and extending outboard across the LEX vortex pressure signatures is also apparent. The shock is revealed as a narrow, swept band of yellow and red colors extending outboard on either side of the tail. The LEX and wing vortex pressure signatures are in proximity, but there is no indication of direct interaction (that is, intertwining of the vortices) or instability of the vortices. It is noted that vortex instability, or breakdown, would not be expected at these test conditions [8] in the absence of large adverse streamwise pressure gradients caused, for example, by high angle of attack, a strong shock wave, or the presence of a solid obstacle in the path of the vortices. The LVS images show two distinct vortex cross sections on either side of the wing centerline: a LEX vortex of nearly circular cross section positioned along the inboard portion of the wing and surrounded by a band of water vapor condensate, and a wing vortex situated along the outer section of the wing which appears as a broader, flatter region of low or negligible water vapor condensate. The wing vortex ‘feeding sheet’ is approximately defined in the LVS images as the boundary between the low condensate region within the vortex and the nearly uniform condensation region outside the vortex. The size of the LEX vortex cross section belies the relatively small pressure signature in the PSP image. The LEX vortex is nearly circular because it is a ‘free’ vortex. It detaches from the leading edge near the LEX-wing junction and does not receive additional leading-edge vorticity as it passes over the wing. The condensate that is entrained between the LEX vortices implies a region of induced downflow that correlates with the higher pressure region in the PSP image. The flatter wing vortex cross section is also consistent with the broader signature in the PSP surface pressure mapping. The LVS images indicate the wing vortex is situated closer to the wing upper surface. In addition, the vortex feeding sheet is attached to the entire wing leading edge. These LVS flow field features correlate with the region of more intense blue and purple colors in the PSP image, which are indicative of higher vortex-induced suction pressures. The LVS images also reveal the presence of condensation between the LEX and wing vortices, which is a region of vortex-induced flow that reattaches to the wing upper surface. This reattached flow region is coded typically a green color in the PSP image and is situated between the boundaries of the LEX and wing vortex pressure footprints. The LVS image near the wing trailing edge ($x/c = 1.00$) reveals the presence of the LEX, wing, and wing tip vortices and a trace of the centerline vertical tail shock. The LVS result at $x/c = 1.00$ supports the inferences from the PSP image, namely, the LEX and wing vortices do not directly interact and the vortices are stable to the wing trailing edge. There is no indication in the LVS image that the traversal of the LEX vortex across the boundary of the shock emanating from the tail causes instability of the vortical flow. The PSP image in fig. 7 corresponding to the porous LEX features a single, broad wing vortex pressure signature on each side of the wing centerline and an absence of the LEX vortex pressure footprints. In addition, regions of higher surface pressures along the forward and central sections of the wing and on either side of the centerline tail are less extensive, which suggest a mitigation of the vortex-induced downflow and a reduction of the shock strength at the tail. Certain trends in the PSP image correlate with the corresponding LVS images, which indicate that LEX porosity shifts the dominance from the LEX vortex to the wing vortex. The singular feature in the

LVS images is a broader, thicker wing vortex cross section compared to its solid LEX counterpart. There is no evidence of the LEX vortices, and the induced downflow above the center portion of the wing is less discernible. No inferences can be made, however, regarding the reduced shock strength at the tail that was suggested in the PSP images.

Fig. 8 presents expanded views of the right-hand portions of the PSP images with solid LEX and porous LEX shown previously in fig. 7. The corresponding LVS flow visualization of the right half of the wing at $x/c = 0.80$ is shown directly below the PSP images. The $x/c = 0.80$ station is denoted as a red dashed line in the PSP image. The PSP and LVS images are scaled relative to the plots of the spanwise distributions of the right-hand wing upper surface static pressure coefficient, C_p , shown at the bottom of the figure. C_p is plotted against the nondimensional semispan location, y/s . Two distributions are shown in each plot corresponding to discrete pressure measurements obtained using the ESP system and from the PSP image which was calibrated via the global in-situ method. The dual vortex pressure footprints and vortex cross sections with the solid LEX correlate with the two pressure signatures in the C_p distributions. One might infer from the relative size of the LEX vortex in the LVS image that the latter would induce a higher suction pressure peak compared to the wing vortex. This is not the case, however, as the PSP pressure map and C_p distributions indicate the LEX vortex induces a minor suction pressure peak compared to the higher suction pressure plateau induced by the broader, flatter wing vortex. The C_p distribution obtained with the porous LEX is shown at the bottom right in fig. 8, which captures a single suction pressure plateau along approximately the outer 60 percent of the wing semispan and an inboard region of increasing pressure (that is, reduced suction pressure). The lateral extent of the suction pressure plateau in the presence of the porous LEX correlates with the broadened vortex pressure signature and vortex cross section in the PSP and LVS images, respectively. In addition, the region of wing vortex-induced flow reattachment inferred from the PSP and LVS images is consistent with the pressure rise inboard of the suction pressure plateau.

Many details of the flow about the 65-degree cropped delta wing can be derived from the combined results obtained using the PSP and LVS techniques. However, results presented so far in fig. 7 and fig. 8 do not clearly identify the effect of flow-through porosity on the LEX vortex system. A technique often used in wind tunnel flow visualization experiments is to perform an angle-of-attack ‘sweep’ from low-to-high values to observe, for example, the development and growth of vortices, vortex interactions, and shock waves. Frequently, the enlarged scale of the flow at higher angles of attack allows one to better discern flow-field features of interest that still exist but are less visible at lower angles of attack. This approach could not be adopted using the PSP method in the UPWT testing, since the optical access required the model to be oriented in a wings-vertical position in the test section and the angle of attack was limited by mechanical operation of the support system to approximately +8 degrees in this orientation. LVS flow visualization was performed with the model in the standard wings-horizontal orientation, and the support system was capable of pitching the model to angles of attack significantly higher than 8 degrees in this plane of motion. Blockage considerations and balance instrumentation load limits at $M = 1.6$ precluded angles of attack greater than approximately 12 degrees. However, these constraints were eased at $M = 2.1$ where the flow-field features were topologically similar to $M = 1.6$ [2]. Fig. 9 shows the LVS cross-flow patterns at $M = 2.1$, $\alpha = 16^\circ$, and $x/c = 0.80$ with the solid LEX and porous LEX. At this higher angle of attack, the LEX and wing vortices are visible in both cases. With the solid LEX, the vortices are distinct and separated, and multiple cross-flow shock waves develop above, between, and below the vortices. With

the porous LEX, the identities of the LEX and wing vortices can still be discerned, but the vortices join to produce a cross flow pattern that is characteristic of a single, broader vortical flow. The LVS image also suggests the combining of the vortices changes the pattern of cross-flow shocks that bound the vortex flows. These results confirm that porosity does not suppress the LEX vortex flows but, instead, causes a diffusion and weakening of the vortices. The phenomena observed at this higher angle and Mach number are expected to exist, albeit to a smaller scale, at the conditions previously shown in fig. 7 and fig. 8. Specifically, the redistribution of the PSP surface pressure response, the LVS cross-flow patterns, and the static pressure coefficient distributions caused by porosity is induced by diffuse, weakened LEX vortices that have combined with stronger and larger wing vortical flows. It is noted that a similar conclusion would likely not have evolved with the exclusive use of the PSP method.

Fig. 10 shows the PSP surface pressure maps and LVS cross-flow images at $M = 1.6$ and $\alpha = 8^\circ$ corresponding to the solid LEX in combination with the centerline vertical tail (depicted on the left) and with twin, wing-mounted vertical tails (depicted on the right). The LVS images were acquired at $x/c = 0.60, 0.80$, and 1.10 , where the latter station is in the near wake of the wing. The centerline and twin vertical tails are positioned downstream of the 80 percent wing chord station, and, their upstream influence at supersonic speeds is limited to disturbances transmitted through the wing boundary layer. As a result, the PSP surface pressure response and LVS cross-flow patterns forward of the tail positions are similar for both tail arrangements, and significant differences are confined to the local regions about the tails and into the near wake. As noted previously in fig. 7, the signature of a shock emanating from the apex region of the centerline tail is apparent in the PSP image, and this shock intersects the pressure footprints of the LEX vortices. The LVS cross-flow pattern at $x/c = 1.10$ reveals the tail shock, which has no apparent effect on the stability of the LEX or wing vortices. A direct interaction of the wing and LEX vortices occurs in the near wake. The wake roll-up and wing tip vortex are also apparent in the LVS image at this station. The PSP and LVS images are more complex in the vicinity of the twin vertical tails. The PSP surface pressure response shows the LEX vortex footprints intersecting the leading edges of the wing-mounted tails. Downstream of this location, the LEX vortex pressure footprints are no longer visible in the PSP image. A strong, intersecting shock system is established between the twin tails, and a rapid pressure rise across the shocks is indicated in the PSP image by the transition from a green color ahead of the shocks, to yellow near the foot of the shocks and, finally, to shades of red and pink downstream of the shock fronts. It is noted that the PSP color display was adjusted during the image processing in an attempt to clearly show the important features in the surface pressure response. In doing so, the paint intensity response in certain small sections of the PSP image would sometimes exceed the extremes of the available color palette, and these saturated regions appear as white or black in the images. The PSP response outboard of the twin tails reveals a swept band of blue and purple colors, which suggests a region of organized flow separation (that is, vortex flows). Outboard of this region, the higher suction pressures induced by the wing leading-edge vortex are manifested as a broad band of blue and purple colors. The LVS image at $x/c = 1.10$ enhances the interpretation of the PSP image. Interestingly, although the PSP image suggests the LEX vortices directly impinge on the vertical tails, the LVS flow visualization shows that the LEX vortices retain their structure and stability into the near wake, even as they traverse through the higher pressure region established downstream of the twin tail shock system. The central region of the LEX vortex is shown as a dark area at about the tail midspan on the inboard side of each vertical tail. The traces of the tail shocks are also evident in the LVS cross-flow pattern. The LVS image confirms the development of a separated flow region containing low or negligible water vapor condensate situated outboard of the

twin tails. The cross flow induced by the LEX vortices at the tails, in combination with the tail leading-edge sweep angle of approximately 45 degrees, may be sufficient to promote a partial-span vortical flow positioned near the junction of the tail and wing upper surface. The presence of this separated flow region limits the inboard lateral growth and movement of the wing leading-edge vortex, which is visible adjacent to the wing tip vortex in the LVS image at $x/c = 1.10$.

A more detailed examination of the flow behavior in the vicinity of the right-hand wing-mounted vertical tail at $M = 1.6$ and $\alpha = 8^\circ$ is provided in fig. 11. PSP static pressure coefficients were extracted from two chordwise rows positioned at nondimensional semispan locations of $y/s = 0.25$ and $y/s = 0.40$ that bounded the right-hand vertical tail. The chordwise distributions of the PSP pressure coefficient at these stations are presented in the plots in the upper left-hand portion of fig. 11, where C_p is plotted versus the pixel number. The first pixel in each row is the closest to the wing leading edge, and the last pixel in each row is closest to the wing trailing edge. The chordwise row at $y/s = 0.25$ has approximately 742 pixels, is positioned inboard of the LEX vortex pressure footprint and the vertical tail, and extends through the high-pressure region downstream of the tail shock. The chordwise row at $y/s = 0.40$ has approximately 632 pixels and is positioned outboard of the vertical tail, intersects the wing leading-edge vortex pressure footprint near the leading edge, and extends through the suction pressure region induced by the hypothesized vortex flow shed from the tail. Both rows are identified as black dashed lines in the PSP image. The chordwise location of the vertical tail apex extended to the two pressure rows corresponds to pixel 587 at $y/s = 0.25$ and pixel 477 at $y/s = 0.40$. Situated directly below and scaled with respect to the PSP image is the corresponding LVS cross-flow pattern in the near wake ($x/c = 1.10$) of the right-hand wing and vertical tail. The PSP pressure distribution at $y/s = 0.25$ is situated near the inboard edge of the LEX vortex pressure footprint, and the corresponding pressure distribution indicates a flow expansion to an approximately constant level along the main portion of the wing up to the region of the vertical tail. A significant flow recompression occurs downstream of the oblique shock wave generated at the tail. The estimated shock front position corresponds to pixel 599 at $y/s = 0.25$. The rapid pressure rise corresponds to the abrupt change in the false-colored PSP image from green to yellow to red/pink across the shock. The pressure row at $y/s = 0.40$ intersects the wing vortex pressure signature near the leading edge, which appears as a blue region in the PSP pressure map. The pressure distribution reveals a corresponding vortex-induced suction pressure peak in this region. The pressure row at $y/s = 0.40$ is situated between the wing and LEX vortex pressure footprints farther aft, and it captures a region of approximately constant pressure level on the wing (depicted as green in the pressure map) up to the vicinity of the vertical tail. The PSP pressure map suggests the presence of a weak shock front extending outboard from the tail, which is consistent with the minor flow recompression shown in the pressure distribution at $y/s = 0.40$. The superposition of a strong vortex flow field in this region reduces the shock strength, however. Farther aft, the pressure distribution reveals a significant increase in the suction pressure level and a well-defined suction pressure peak that is approximately centrally located in a region of blue and purple colors in the PSP pressure map. The transition from green to blue colors at $y/s = 0.40$ in the PSP image occurs at approximately pixel 485. The pressure distribution and false-colored pressure map in this region are consistent with the induced effects of a vortex flow emanating from the vertical tail. The LVS image in the near wake of the wing confirms the presence of this vortex situated at the outboard junction of the tail and wing upper surface. The tail vortex appears as a dark region with essentially no water vapor condensate surrounded by a lighter region of condensation.

5.2 Generic Double Delta Wing

The PSP and LVS images obtained on the double delta wing model at $M = 0.85$ and $M = 1.20$ are shown in fig. 12 corresponding to $\alpha = 20^\circ$. PSP color bars are not presented for the double delta wing since the intensity ratio scales and corresponding color coding were tailored to each angle of attack and Mach number to extract important features of the surface pressure field response. Specification of a common intensity ratio scale for all angles of attack and Mach numbers would have resulted in large, uninterpretable white or black regions in certain images. The comparisons of the PSP images are solely intended to illustrate significant qualitative differences caused by Mach number changes at the selected angles of attack. In general, blue, lavender, and purple colors correspond to regions of low pressure (high suction pressure coefficients), whereas regions of higher surface pressures are represented by yellow and red colors. A green color corresponds to an intermediate suction pressure level. The LVS cross-flow patterns are presented directly below the PSP images with which they are associated. LVS images obtained at $x/c = 0.25$, 0.75 , and 0.90 are shown, where x is the distance measured along the model centerline beginning at the strake apex. These locations correspond to pressure measurement stations where discrete pressure tap data were acquired in spanwise rows along the left strake and wing upper surfaces. The PSP image at $M = 0.85$ reveals the pressure signature of the strake vortex beginning near the strake apex and extending to nearly the 90 percent chord station. The intensity of the strake vortex pressure signature is highest in a region beginning near the strake-wing junction to approximately the 75 percent chord station. This region is denoted by colors ranging from lavender to purple. The vortex that is shed from the wing leading edge is stronger than the strake vortex [9], and it induces significant suction pressures over a portion of the wing upper surface. However, the vortex feeding sheet does not remain attached to the leading edge because of the moderate wing sweep and the induced effect of the strake vortex. As a result, the wing vortex moves inboard and upward away from the surface [3], and its induced effect on the wing surface pressure field diminishes. The strake vortex is no longer fed by leading-edge vorticity downstream of the strake-wing junction, yet its surface pressure footprint is most intense in this region. This effect may be caused by a downward displacement toward the wing surface as a result of its interaction with the wing vortex. Downstream of approximately the 90 percent chord station, the pressure signatures of the strake and wing vortices are diffuse or indistinct. This trend is consistent with the onset of vortex breakdown upstream of the wing trailing edge. The presence of an apparent normal shock wave situated between the 75 percent and 90 percent chord stations and centered on the wing may contribute to the speculated vortex instability. The shock presence is inferred from the abrupt color change from green to yellow to red, and the spanwise extent of the shock may be limited by a three-dimensional relief effect induced by the presence of strong vortical flows over the wing [10]. The LVS images at $x/c = 0.25$ and $x/c = 0.75$ reveal a stable ‘donut-shaped’ strake vortex cross section in proximity to the upper surface, which correlates with the strong pressure signature in the PSP image. The discontinuous band of condensate above the vortex at $x/c = 0.75$ is interpreted as a discontinuity in the vortex feeding sheet. The wing vortex is not visible in the LVS flow visualization at $M = 0.85$ because of insufficient local condensation. In contrast, more water vapor condensate accumulates within the strake vortex making it highly visible. This may be related to the long run length along which leading-edge vorticity sheds and feeds into the strake vortex before it passes over the wing upper surface. The onset of vortex breakdown inferred from the PSP image is confirmed in the LVS cross-flow patterns at $x/c = 0.90$, where the vortex has expanded and the core region has filled with water vapor condensate.

A notable transformation occurs in the PSP image at $M = 1.20$ relative to $M = 0.85$ as shown on the right-hand side of fig. 12. Increasing the Mach number from 0.85 to 1.20 weakens the leading-edge vortices and reduces the adverse longitudinal pressure gradient through which the vortices must traverse [10]. Direct vortex interaction and normal shock effects that occur at the lower Mach number are mitigated or eliminated at the higher Mach number, and the vortices will persist in a stable form to higher angles of attack. The PSP image at $M = 1.20$ captures distinct strake and wing vortex pressure signatures that persist to the wing trailing edge. Direct interaction, or intertwining, of the strake and wing vortices does not occur at this Mach number. The PSP image suggests the wing vortex feeding sheet remains attached to the leading edge to nearly the wing tip. Furthermore, the normal shock footprint observed at $M = 0.85$ is eliminated at $M = 1.20$. The LVS cross-flow patterns at $M = 1.20$ are consistent with the trends in the PSP image and also reveal a transformation of the condensation patterns compared to $M = 0.85$. Condensation at the higher Mach number first appears in the free stream, so the vortical flows are visible as dark regions in the absence of scattered light surrounded by a light background. The LVS cross-flow patterns reveal a juxtaposition of stable strake and wing vortices. The strake vortex is approximately circular in cross section, becoming less so further aft on the wing, whereas the wing vortex is a flattened, elliptically-shaped region that appears attached to the leading edge. The attachment of the feeding sheet is assumed when the narrow band of condensate along the outer edge of the wing vortex is attached to the leading edge.

Expanded views of the PSP surface pressure response on the left-hand strake and wing upper surface at $M = 0.50$ and $M = 1.20$ are presented in fig. 13 corresponding to $\alpha = 20^\circ$. The corresponding LVS cross-flow patterns about the left-hand wing at $x/c = 0.75$ are also shown directly below the PSP images. The PSP and LVS images are scaled relative to each other and, also, to the plots of the spanwise C_p distributions on the left wing at $x/c = 0.75$ shown at the bottom of fig. 13. The pressure distributions were obtained using the ESP and PSP techniques. Note that the C_p distributions are plotted to different scales at $M = 0.50$ and $M = 1.20$. Fig. 13 provides representative results obtained at a lower subsonic Mach number and at a higher transonic Mach number to highlight the different flow topologies encountered across the range of Mach number in the 8-Foot TPT testing. The PSP image at $M = 0.50$ and $\alpha = 20^\circ$ reveals the strake vortex pressure signature highlighted in blue-to-lavender colors that persists just downstream of the 75 percent chord station. The PSP intensity field response to the strake vortex is highest near the strake-wing intersection, where the strake vortex is drawn closer to the wing surface as a result of an interaction with the wing vortical flow. The wing vortex pressure footprint is visible near the strake-wing intersection as a region of blue, lavender, and purple colors, but this footprint quickly becomes obscured as the vortex detaches from the leading edge and interacts with the dominant strake vortex. Downstream of the 75 percent chord station, the intensity of the combined strake and wing vortex footprint diminishes, and the expanding region of yellow and red colors along the aft portion of the wing suggests the onset of vortex breakdown. The LVS cross-flow image at $x/c = 0.75$ reveals a stable, donut-shaped strake vortex, which is consistent with the PSP pressure field response at this station. The LVS pattern also shows a cloud of water vapor condensate outboard of and above the strake vortex, which is interpreted as a burst wing vortex flow, thereby obscuring the wing vortex footprint in the PSP image. The flow situation inferred from the PSP and LVS images at $M = 0.50$ leads to the single-peaked pressure distribution at the bottom of fig. 13, where the spanwise location of the suction pressure peak correlates with the positions of the strake vortex pressure footprint in the PSP color mapping and the condensation pattern in the LVS image. The significantly diminished suction pressure level along approximately the outer 40 percent of the local semispan is attributed to

the occurrence of wing vortex breakdown. The salient features of the PSP image at $M = 1.20$ and $\alpha = 20^\circ$ in fig. 13 include well-defined strake and wing vortex pressure signatures that are independent and persist to the wing trailing edge. The independence of the signatures implies no direct interaction between the vortical flows, and from their persistence one can infer stability. The character of the pressure signatures suggests the wing vortex is very broad compared to the strake vortex. Inferences from the PSP image are supported by the LVS cross-flow pattern at $x/c = 0.75$, and the flow topology in the PSP and LVS images is consistent with the pressure coefficient distribution at $x/c = 0.75$. The spanwise C_p distribution shows a pronounced suction pressure peak correlating with the location of the strake vortex in the PSP and LVS images and, farther outboard, a broader distribution featuring a maximum suction pressure plateau that correlates with the flatter, elliptically-shaped wing leading-edge vortex.

5.3 Faceted Missile Model

PSP and LVS images obtained on the faceted missile model at $M = 1.20$ are shown in fig. 14 corresponding to $\alpha = 12^\circ$ and $\alpha = 20^\circ$. The size of the PSP images shown at the top of fig. 14 are different at the two angles of attack, since the facility arc sector support mechanism pitched the model closer to the PSP image acquisition camera installed in the test section ceiling as the angle of attack was increased from 12° to 20° . The LVS flow visualization results correspond to M.S. 20.40, 25.50, and 30.00 expressed in inches measured from the nose tip of the 36-inch-long model. Discrete pressure tap data were obtained in spanwise rows at these stations using the ESP method. The LVS images are scaled relative to each other but not to the PSP images.

The PSP intensity field response is more subtle on the faceted missile model compared to the 65-degree cropped delta wing-LEX and double delta wing models discussed in previous sections of this paper. The slender forebody, forward-swept aftbody, thick diamond-shaped cross sections, and large chine included angles at the leading edges diminish the strength of the vortical flows compared to the thin, sharp-edge, less highly-swept wings. In addition, the slender missile model is more prone to flow-field asymmetries at zero sideslip angle (β), which is apparent in the PSP images particularly along the aftbody region. A PSP color bar is included in fig. 14 which indicates that regions of higher suction pressures are coded green, blue, and purple, and regions of lower suction pressures or small positive pressures are represented by shades of yellow, red, and pink. The footprints of the forebody vortices at $\alpha = 12^\circ$ are initially discernible in the PSP image as narrow green bands along the forebody, which intensify to blue color along the transition section of the body. The vortex footprints appear to widen along the aftbody, albeit in an asymmetric fashion relative to the model centerline, and the lighter green and yellow color coding is indicative of diminished influence of the vortices on the surface pressures. A small region of dark blue color is also apparent near the planform break, which suggests a second region of organized flow separation. The off-surface flow field at $\alpha = 12^\circ$ is dominated by the vortex pair shed from the forebody as shown in the LVS cross-flow patterns in fig. 14. The scale of the vortex structure in the LVS flow visualization contrasts with the relatively subtle surface pressure signatures in the PSP image, particularly along the aftbody region. A band of condensation connects each vortex to the body edge at M.S. 20.40, which indicates the feeding sheet is attached to the leading edge. The body chine is essentially a trailing edge downstream of the planform break, and it is presumed that vorticity is no longer feeding into the vortex from this point aft. Consequently, the flow about the afterbody section is characterized by a free vortex system. An interesting feature of the LVS cross-

flow patterns at M.S. 25.50 and 30.00 is the development of a second pair of smaller, co-rotating vortices that directly interact with the forebody vortical flows. It is speculated that a discontinuity exists in the forebody leading-edge vortex shear layer upstream of the planform break. The premature detachment of the forebody vortex feeding sheet from the body edge upstream of the planform break allows a second pair of co-rotating vortices to form along the transition region. A strong interaction of the co-rotating vortices occurs along the aftbody as shown in the LVS pattern at M.S. 30.00. The vortex system is no longer attached to the model via a leading-edge feeding sheet in this region and, therefore, it migrates away from the upper surface. This upward displacement is a plausible explanation for the diminished surface pressure signature along the aft portion of the model. The flow topology in the PSP and LVS images at $\alpha = 20^\circ$ shown on the right-hand side of fig. 14 is similar to that observed at $\alpha = 12^\circ$. Increasing the angle of attack amplifies the forebody vortex pressure signature and the scale of the vortex cross-flow patterns in the PSP and LVS images, respectively. The LVS condensation patterns are dominated by the forebody primary vortices, and the influence of the second pair of co-rotating vortices is significantly diminished at the higher angle of attack. The streamwise accumulation of water vapor condensate on the long slender model creates a vivid depiction of the vortical flows. However, the scale and complexity of the vortex-dominated condensation patterns along the aftbody are incongruous with the relatively subtle features in the PSP surface pressure response.

The PSP images and selected LVS cross-flow patterns at $M = 1.20$ corresponding to $\alpha = 12^\circ$ and $\alpha = 20^\circ$ in fig. 14 are expanded in fig. 15 for comparison to the upper surface static pressure coefficient distributions at M.S. 25.50. Only the LVS images are appropriately scaled to the C_p distributions shown at the bottom of the figure. Straightforward correlations are made between the spanwise locations of the forebody primary vortices and the suction pressure peaks at $\alpha = 12^\circ$ and $\alpha = 20^\circ$. The presence of the second pair of co-rotating vortices at $\alpha = 12^\circ$ is not manifested in the pressure distributions, although they are clearly visible in the LVS image. The influence of the relatively large regions of secondary separation denoted in the LVS image at $\alpha = 20^\circ$ is associated with inflection points in the pressure distributions outboard of the primary vortex suction peaks.

Fig. 16 shows the effect of sideslip on the PSP surface pressure response and LVS cross-flow patterns at $M = 0.90$ and $\alpha = 20^\circ$. The forebody primary vortex pressure signatures at $\beta = 0^\circ$ appear as narrow bands of blue color that are symmetrically positioned along the forebody and broader bands of green color that are asymmetrically disposed along the rear portion of the aftbody. A secondary region of locally high suction pressures is coded dark blue in the transition section of the body, which is similar to the pattern observed at $M = 1.20$ and $\alpha = 20^\circ$ in fig. 14 and fig. 15. The LVS patterns at $\beta = 0^\circ$ reveal a symmetric pair of forebody vortices at M.S. 20.40 and the development of a second pair of smaller vortices rotating in the same sense at M.S. 25.50 that is presumed to originate from the transition region. The latter vortex pair is entrained into the dominant forebody vortices, and they appear as spiral discontinuities at the outer edge of the vortex cross-flow images at M.S. 30.00. As a consequence, the presence of the co-rotating vortex pair is not manifested in the PSP image. There is some evidence of vortex asymmetry at M.S. 25.50 and 30.00, where the right-hand vortex system is situated slightly higher above the surface. The PSP image at $\beta = -2.5^\circ$ (nose right) in fig. 16 reveals a pressure signature of the left-hand, or windward, forebody vortex, which is discernible as a narrow band of blue and dark green colors over most of the body length. In addition, there is a second region

of higher suction pressures coded dark blue/purple on the windward side along the transition region of the body. In contrast, the pressure signature of the forebody vortex on the right-hand, or leeward, side is less visible along the forebody region and barely discernible along the aftbody. Good qualitative correlation exists between the PSP and LVS images. At M.S. 20.40, for example, the windward forebody vortex is close to the surface and is attached to the leading edge by a band of condensate. The leeward vortex is situated farther above the surface, and there is no evidence of a feeding sheet connecting the vortex to the leading edge at this model station. In sideslip, the windward vortex moves closer to the model surface while the leeward vortex migrates away from the surface [4]. This effect contributes to the higher PSP suction pressure levels on the windward side compared to the leeward side. In addition, the effective decrease in the leading-edge sweep on the windward side yields a stronger vortex at a given angle of attack, whereas the opposite effect occurs on the leeward side [9]. The development of a second, co-rotating vortex is apparent at M.S. 25.50 from the transition region of the body on the windward side. This smaller, weaker vortex is observed to orbit about the dominant forebody vortex at M.S. 30.00, which remains in proximity to the model surface. The latter trend is consistent with the persistence of the vortex pressure signature in the PSP image. By comparison, the apparent free vortex system on the leeward side induces a more subtle pressure signature.

The PSP false-colored pressure maps and the LVS images at M.S. 25.50 from fig. 16 are expanded in fig. 17 for comparison to the spanwise C_p distributions at M.S. 25.50 corresponding to $\beta = 0^\circ$ and $\beta = -2.5^\circ$. The LVS images are approximately scaled to their respective C_p distribution plots. The locations of the bands of green/blue color in the PSP pressure map and the forebody vortex cross-flow patterns in the LVS image at $\beta = 0^\circ$ correlate with the suction pressure peak locations in the C_p plot at the bottom left of fig. 17. The aftbody flow asymmetry noted in fig. 16 at $\beta = 0^\circ$ is manifested as a slight asymmetry in the magnitude of the peak C_p values. The presence of the second pair of co-rotating vortices visible in the LVS cross-flow pattern does not project to the C_p plot, because of their spatial locations relative to the model surface and the dominance of the forebody vortices. The significant asymmetries that are imposed on the PSP and LVS images due to sideslip correlate very well with the corresponding C_p plot at $\beta = -2.5^\circ$ at the bottom right of fig. 17. The stronger windward vortex in proximity to the upper surface induces a much higher suction pressure peak compared to its weaker leeward counterpart that is positioned higher above the model.

6 Summary

Laser vapor screen flow visualization and pressure-sensitive paint techniques were applied in a tandem approach to investigate the vortex- and shock wave-dominated flow fields about slender wing and missile configurations at subsonic, transonic, and supersonic speeds. Selected results were presented from experiments performed on 65-degree cropped delta wing-LEX, double delta, and faceted missile models in the NASA Langley Research Center Unitary Plan Wind Tunnel and the 8-Foot Transonic Pressure Tunnel. The LVS technique was considered qualitative, since the appearance of condensation in the test section affects the free-stream flow characteristics. The potential intrusive effects of PSP were mitigated by controlling the thickness and surface roughness of the luminescent paint coating. Within these constraints, however, the LVS cross-flow patterns were effectively projected to the false-colored PSP surface pressure maps to identify the salient features of the aerodynamic flows about the selected models. The LVS and PSP techniques were complementary in that they provided a more

complete depiction of the complex three-dimensional flow fields that were characterized by the development and interaction of multiple leading-edge vortices and shock waves, vortex breakdown, and vortex interactions with vertical tail surfaces. The combination of these techniques was also a powerful tool in visualizing and quantifying the effects of passive surface porosity on vortex flow development and interactions. The application of the LVS and PSP techniques was mutually exclusive, because of the different requirements for the optical components, model surface preparation, and wind tunnel test conditions. Consequently, the LVS and PSP results were obtained in separate phases in each experiment, which required appropriate test planning and efficient use of wind tunnel facility resources. The successive application of these techniques often yielded synergistic results, however, since certain flow features that were subtle or not discernible using one technique were often clearly revealed using the other.

7 References

1. Erickson G E. Overview of Supersonic Aerodynamics Measurement Techniques in the NASA Langley Unitary Plan Wind Tunnel. NASA TM-2007-214894, 2007.
2. Erickson G E. Wind Tunnel Investigation of the Effects of Surface Porosity and Vertical Tail Placement on Slender Wing Vortex Flow Aerodynamics at Supersonic Speeds. NASA TM-2007-215082, 2007.
3. Erickson G E and Gonzalez H A. Wind Tunnel Application of a Pressure-Sensitive Paint Technique to a Double Delta Wing Model at Subsonic and Transonic Speeds. NASA TM-2006-214319, 2006.
4. Erickson G E. Wind Tunnel Application of a Pressure-Sensitive Paint Technique to a Faceted Missile Model at Subsonic and Transonic Speeds. NASA TM-2004-212991, 2004.
5. Amer T R, Liu T and Oglesby D M. Characterization of Pressure Sensitive Paint Intrusiveness Effects on Aerodynamic Data. AIAA 2001-0556, 39th AIAA Aerospace Sciences Meeting & Exhibit, Reno, NV, 2001.
6. Jackson C M, Corlett W A and Monta W J. Description and Calibration of the Langley Unitary Plan Wind Tunnel. NASA TP 1905, 1981.
7. Brooks C W Jr., Harris C D and Reagon P G. The NASA Langley 8-Foot Transonic Tunnel Calibration. NASA TP 3437, 1994.
8. Wood R M. Supersonic Aerodynamics of Delta Wings. NASA TP 2771, 1988.
9. Hemsch M J and Luckring J M. Connection Between Leading-Edge Vortex Lift and Vortex Strength for Delta Wings. *Journal of Aircraft*, Vol. 27, No. 5, pp. 473-375, 1990.
10. Erickson G E. Wind Tunnel Investigation of the Interaction and Breakdown Characteristics of Slender-Wing Vortices at Subsonic, Transonic, and Supersonic Speeds. NASA TP-3114, 1991.

Copyright Statement

The author confirms that NASA holds copyrights on all of the original material included in this paper. This paper does not contain any third party material. The author grants full permission for the publication and distribution of this paper as part of the ISFV13/FLUVISU12 proceedings or as individual off-prints from the proceedings.

UNIFIED APPLICATION OF VAPOR SCREEN FLOW VISUALIZATION AND PRESSURE SENSITIVE PAINT MEASUREMENT TECHNIQUES TO VORTEX- AND SHOCK WAVE-DOMINATED FLOW FIELDS

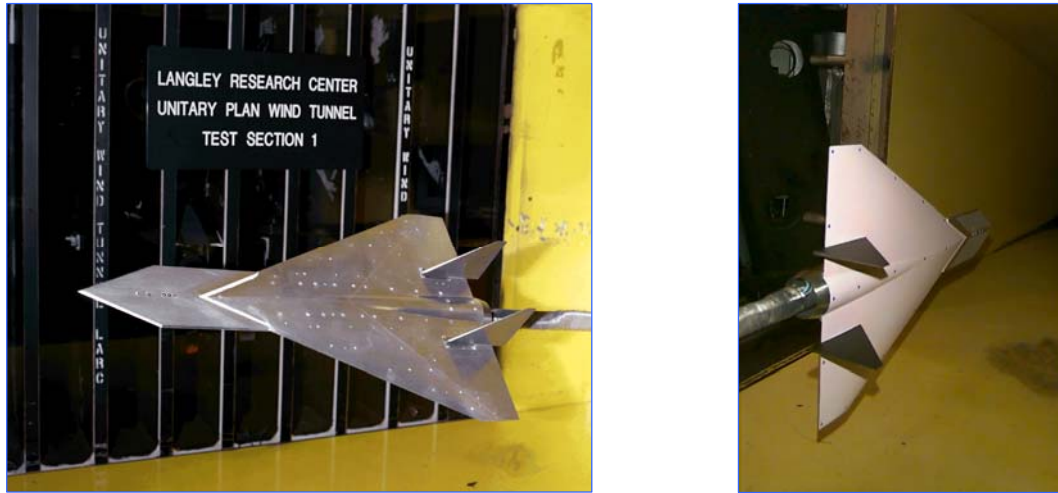
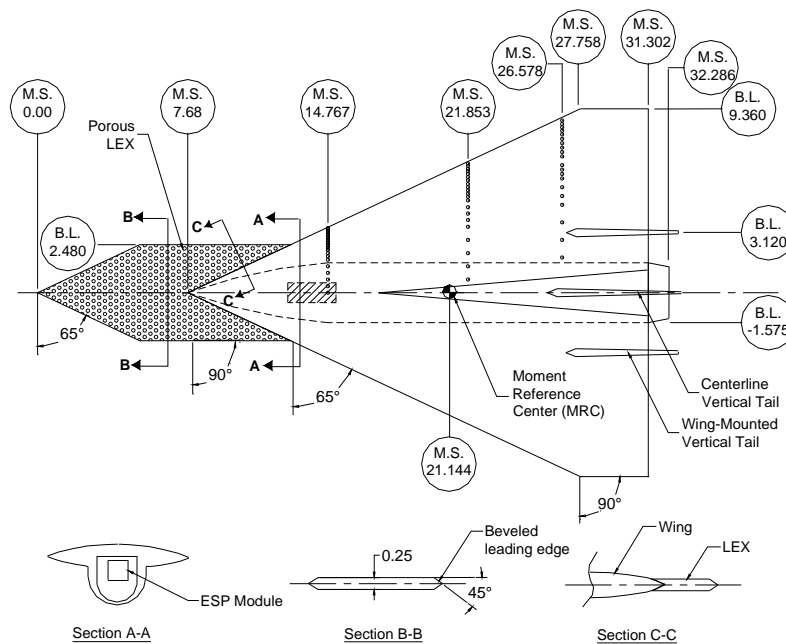
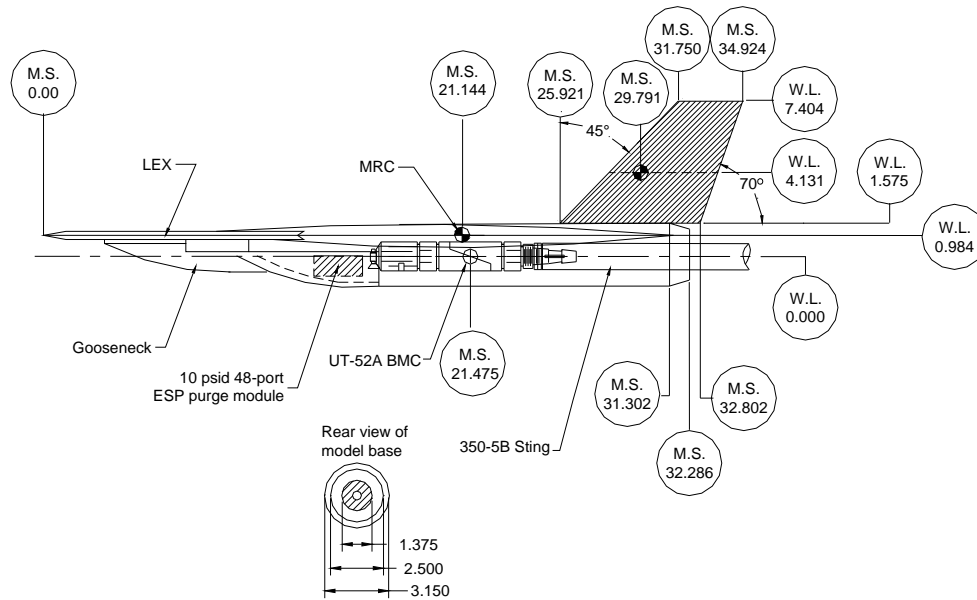


Fig. 1. Photographs of the 65-degree cropped delta wing-LEX model installed in Test Section 1 of the NASA Langley Research Center Unitary Plan Wind Tunnel (photograph to the right shows the model prepared for PSP testing)



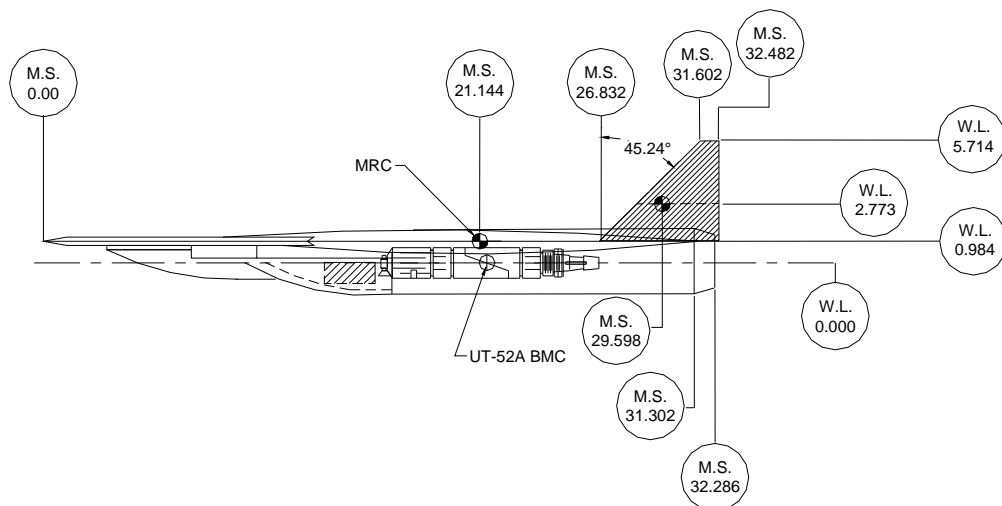
(a) planview

Fig. 2. Details of the 65-degree cropped delta wing-LEX model (all dimensions in inches) (B.L. = butt line, BMC = balance moment center, M.S. = model station, MRC = moment reference center, W.L. = water line)



(b) sideview with centerline vertical tail

Fig. 2. Continued



(c) sideview with twin vertical tails

Fig. 2. Concluded

UNIFIED APPLICATION OF VAPOR SCREEN FLOW VISUALIZATION AND PRESSURE SENSITIVE PAINT MEASUREMENT TECHNIQUES TO VORTEX- AND SHOCK WAVE-DOMINATED FLOW FIELDS

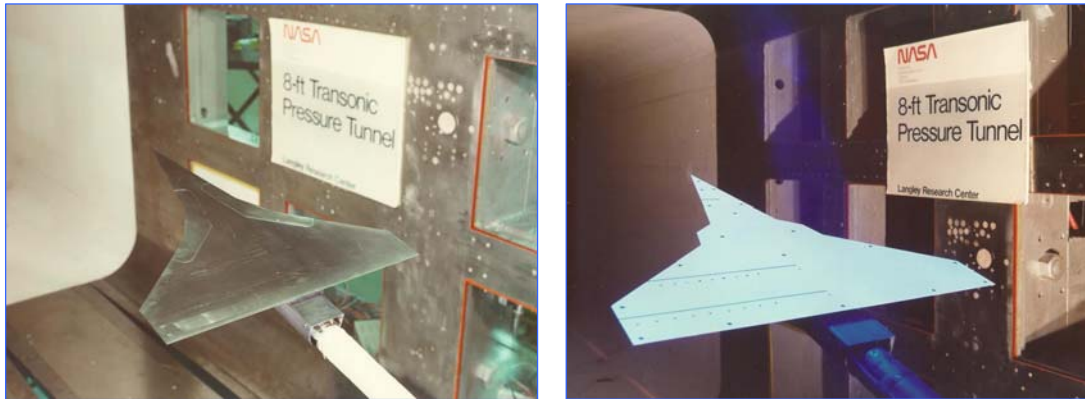


Fig. 3. Photographs of the double delta wing model installed in the test section of the NASA Langley Research Center 8-Foot Transonic Pressure Tunnel (photograph to the right shows the model prepared for PSP testing)

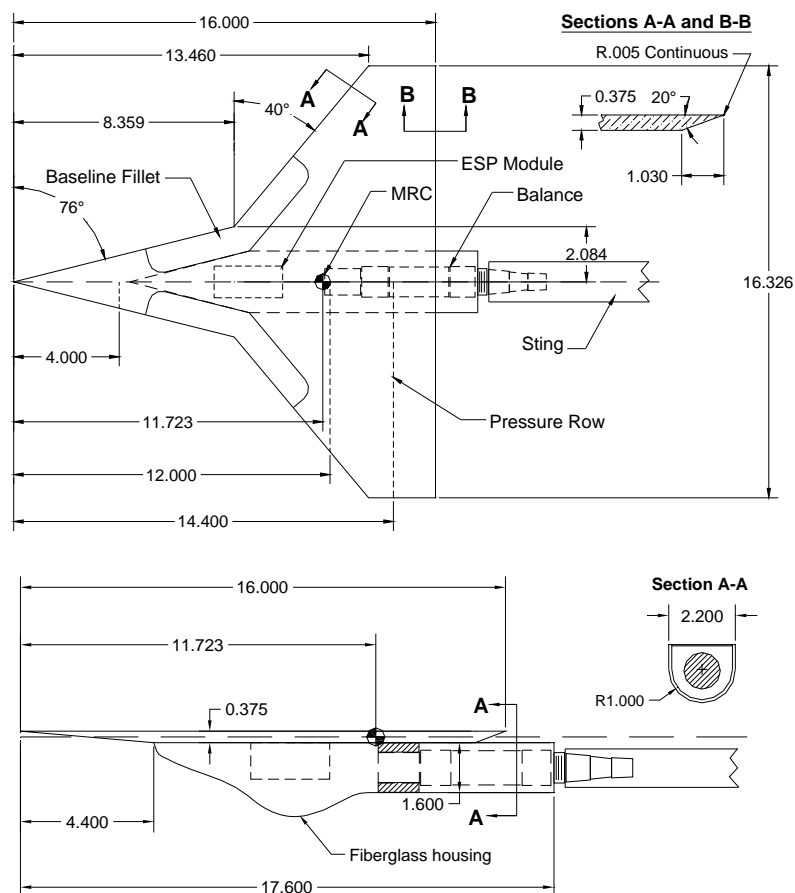


Fig. 4. Planview and sideview of the double delta wing model (all dimensions in inches)



Fig. 5. Photographs of the faceted missile model installed in the test sections of NASA Langley Research Center wind tunnels (photograph to the right shows the model in the NASA LaRC 8-Foot TPT prepared for PSP testing)

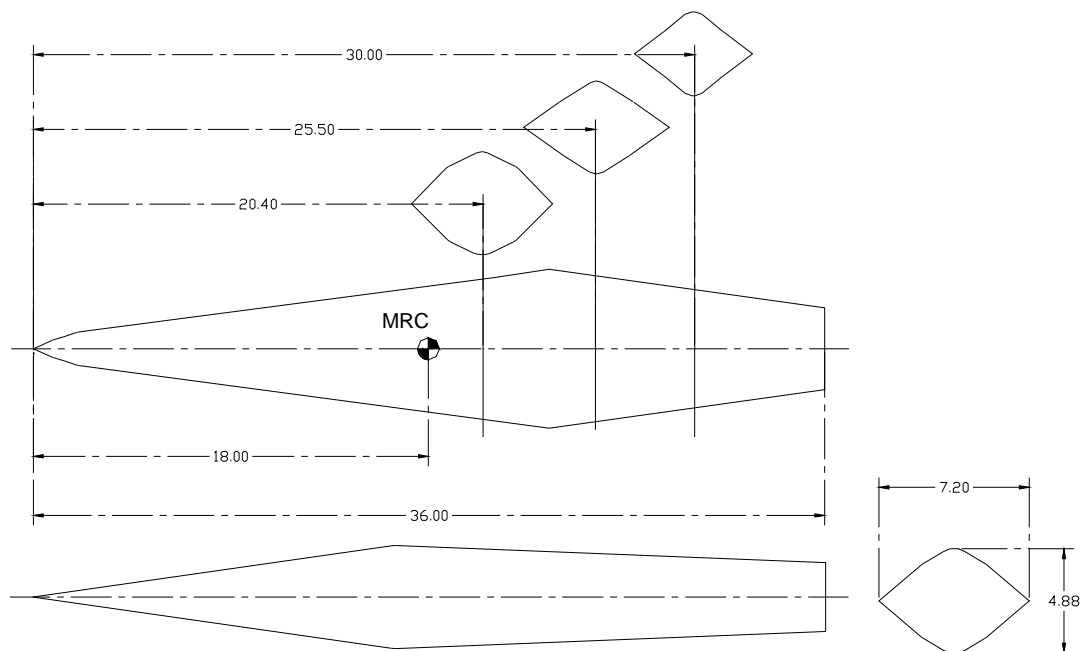


Fig. 6. Details of the faceted missile model (all dimensions in inches)

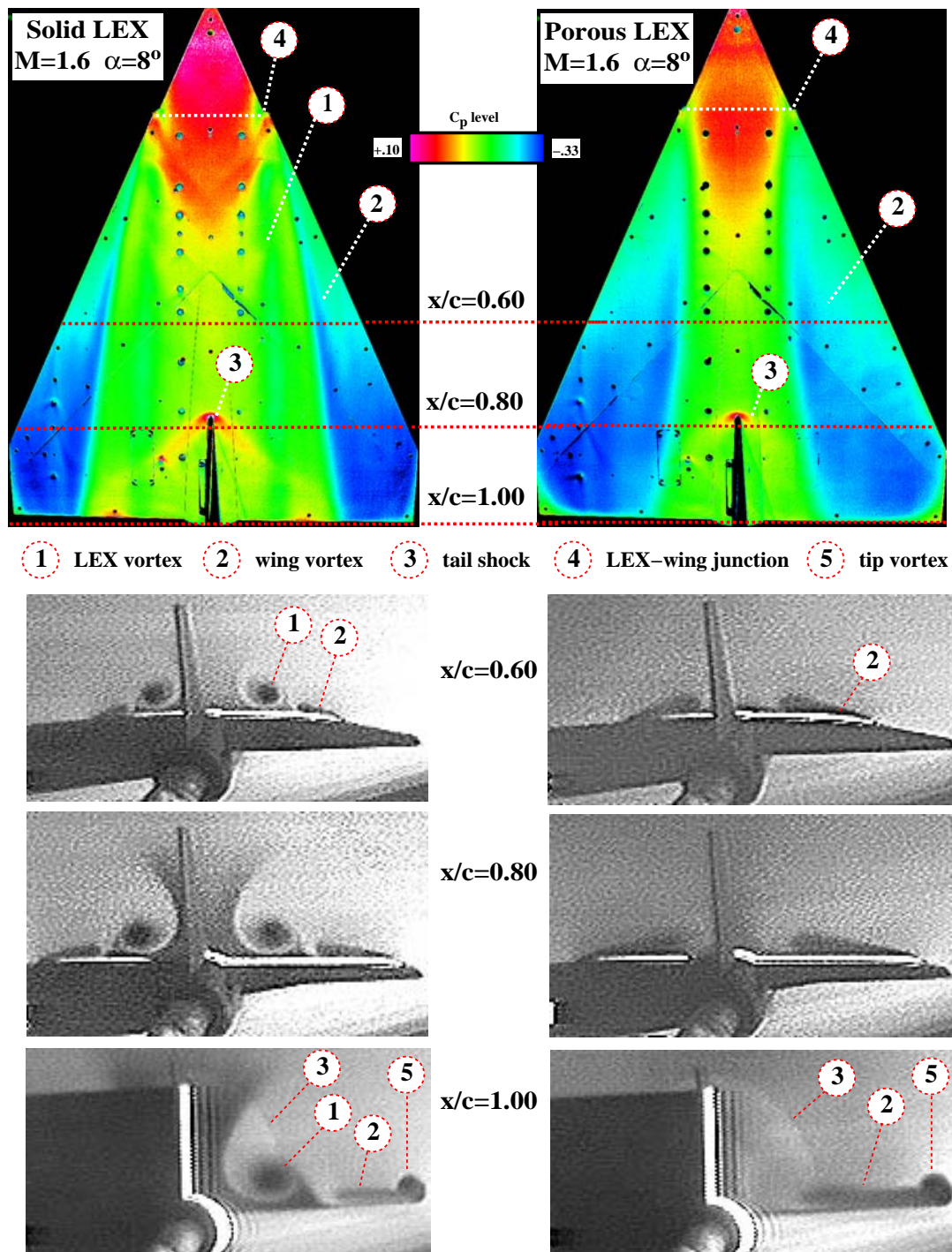


Fig. 7. Comparison of PSP and LVS images on the 65-degree cropped delta wing model with solid LEX and porous LEX at $M = 1.6$, $\alpha = 8^\circ$

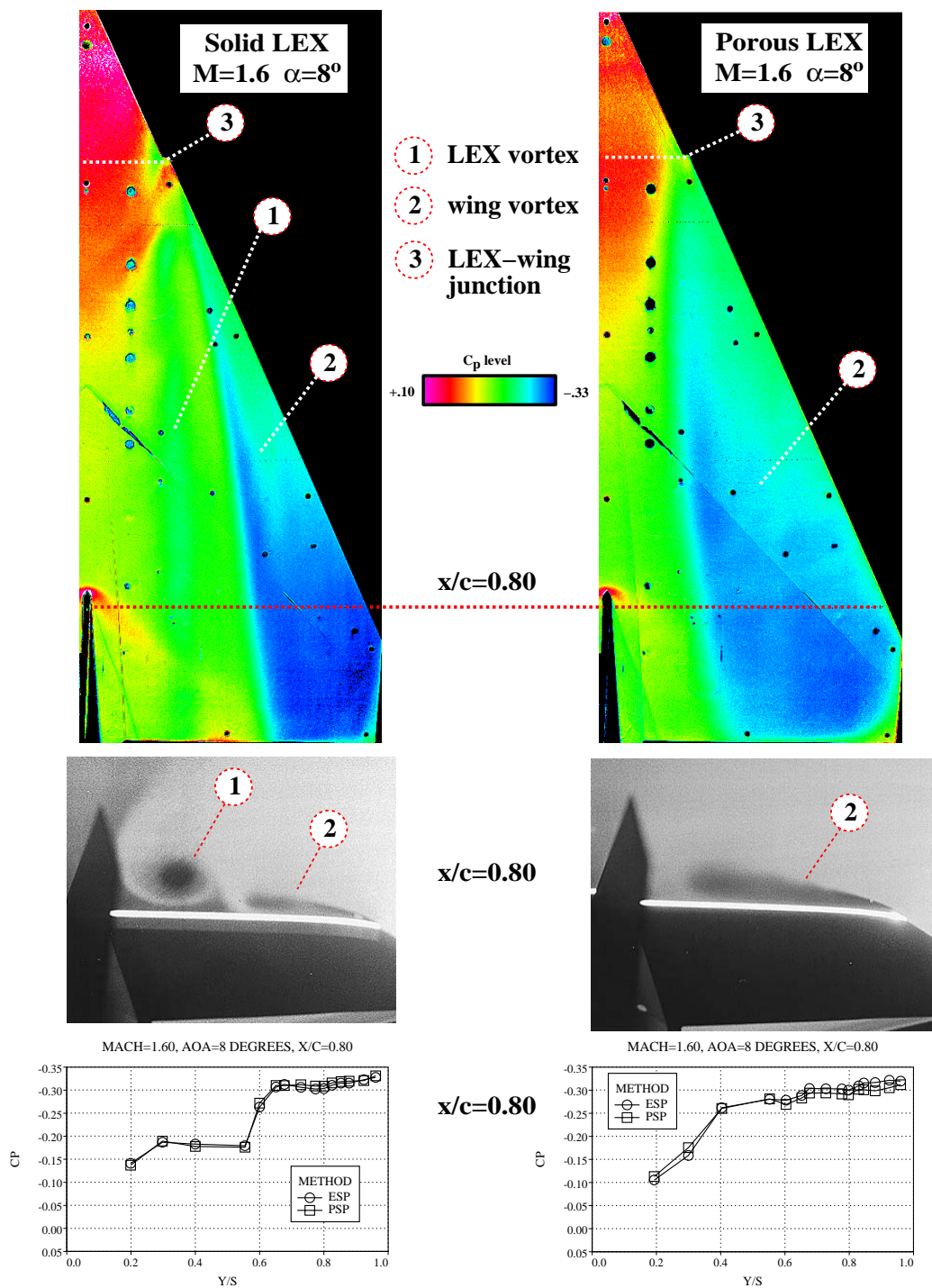


Fig. 8. Correlation of PSP and LVS images with spanwise pressure distributions on the 65-degree cropped delta wing model with solid LEX and porous LEX at $M = 1.6$, $\alpha = 8^\circ$

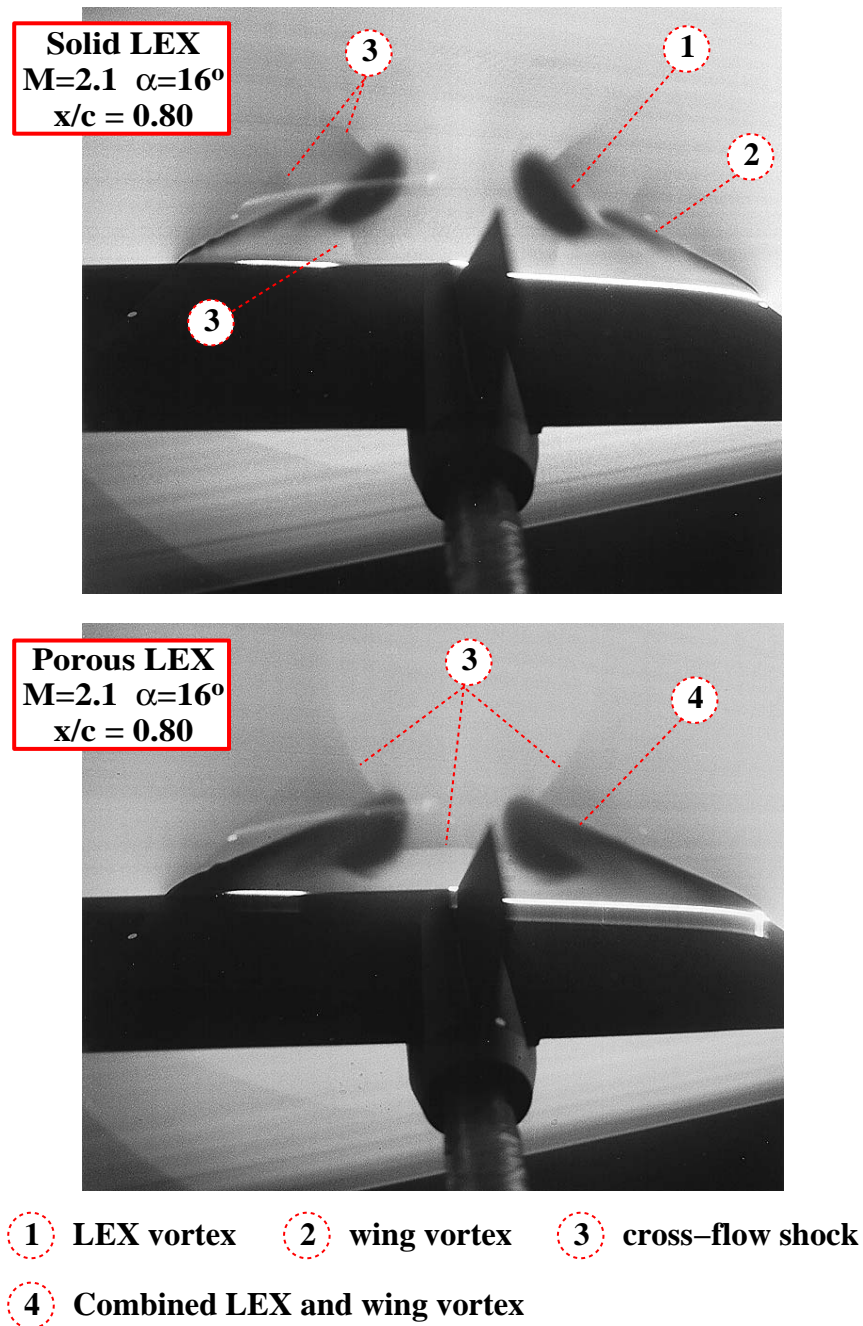


Fig. 9. Comparison of LVS images on the 65-degree cropped delta wing model with solid LEX and porous LEX at $M = 2.1$, $\alpha = 16^\circ$

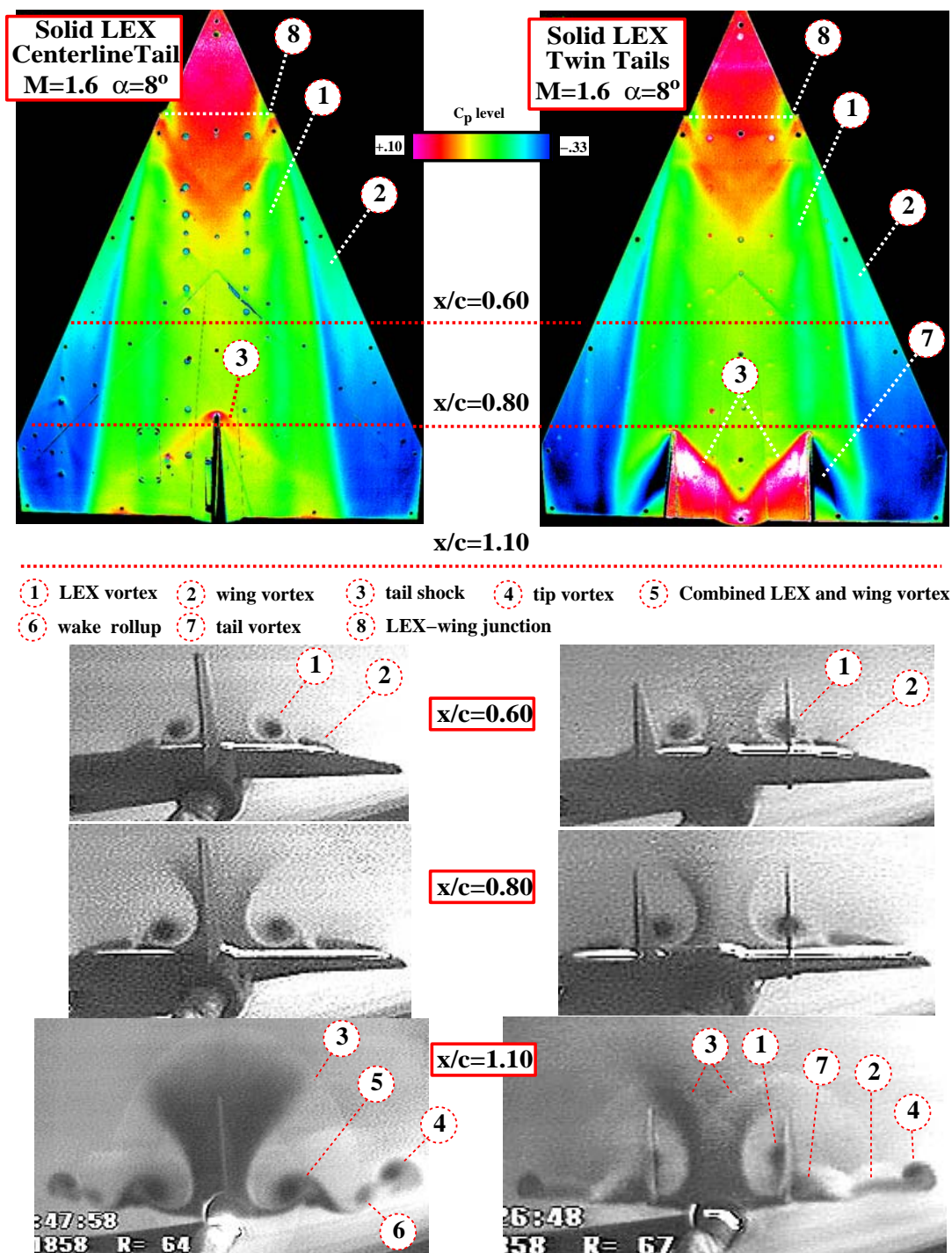


Fig. 10. Comparison of PSP and LVS images on the 65-degree cropped delta wing model with solid LEX and centerline and twin vertical tails at $M = 1.6$, $\alpha = 8^\circ$

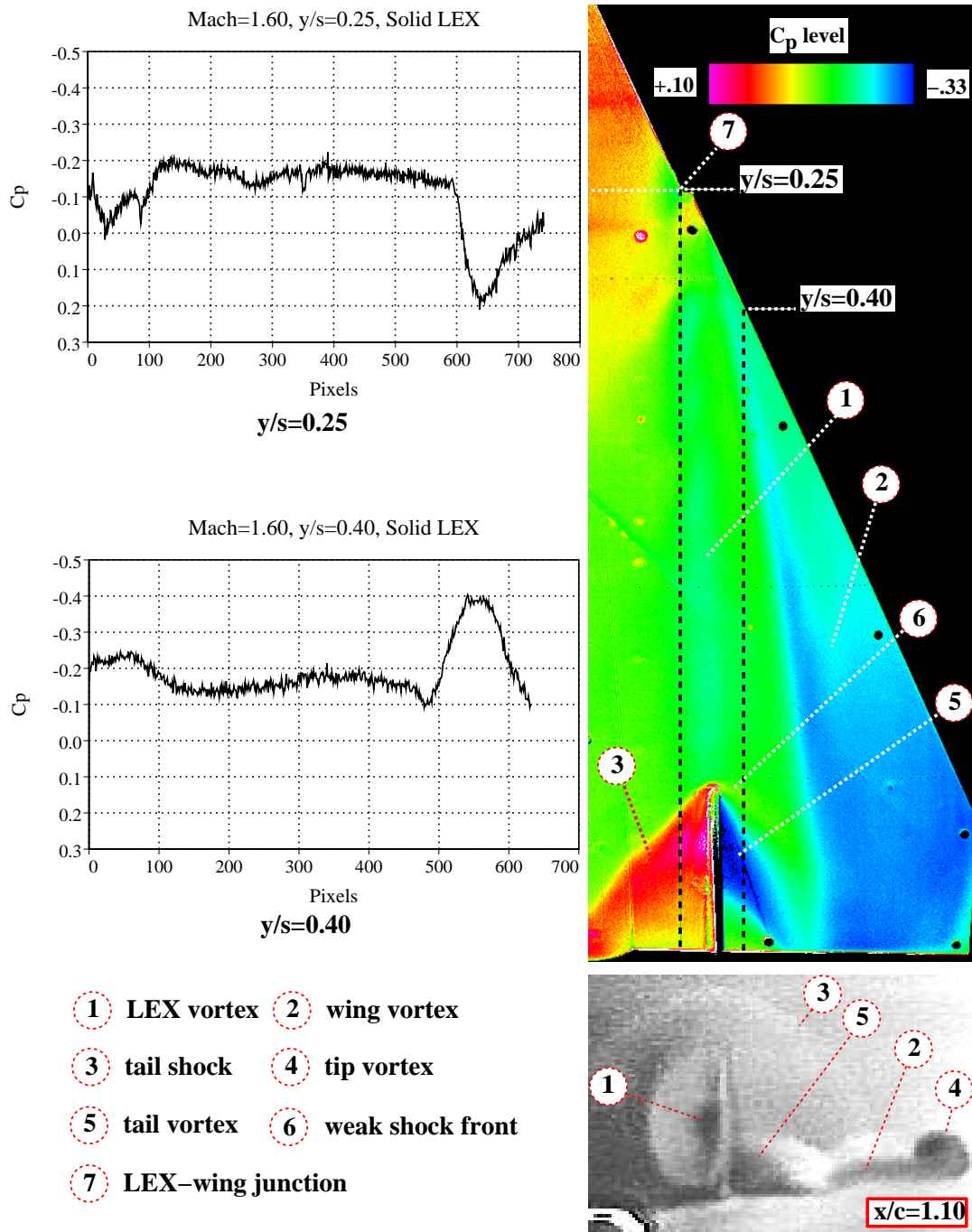


Fig. 11. Correlation of PSP and LVS images with chordwise pressure distributions on the 65-degree cropped delta wing model with solid LEX and twin vertical tails at $M = 1.6$, $\alpha = 8^\circ$

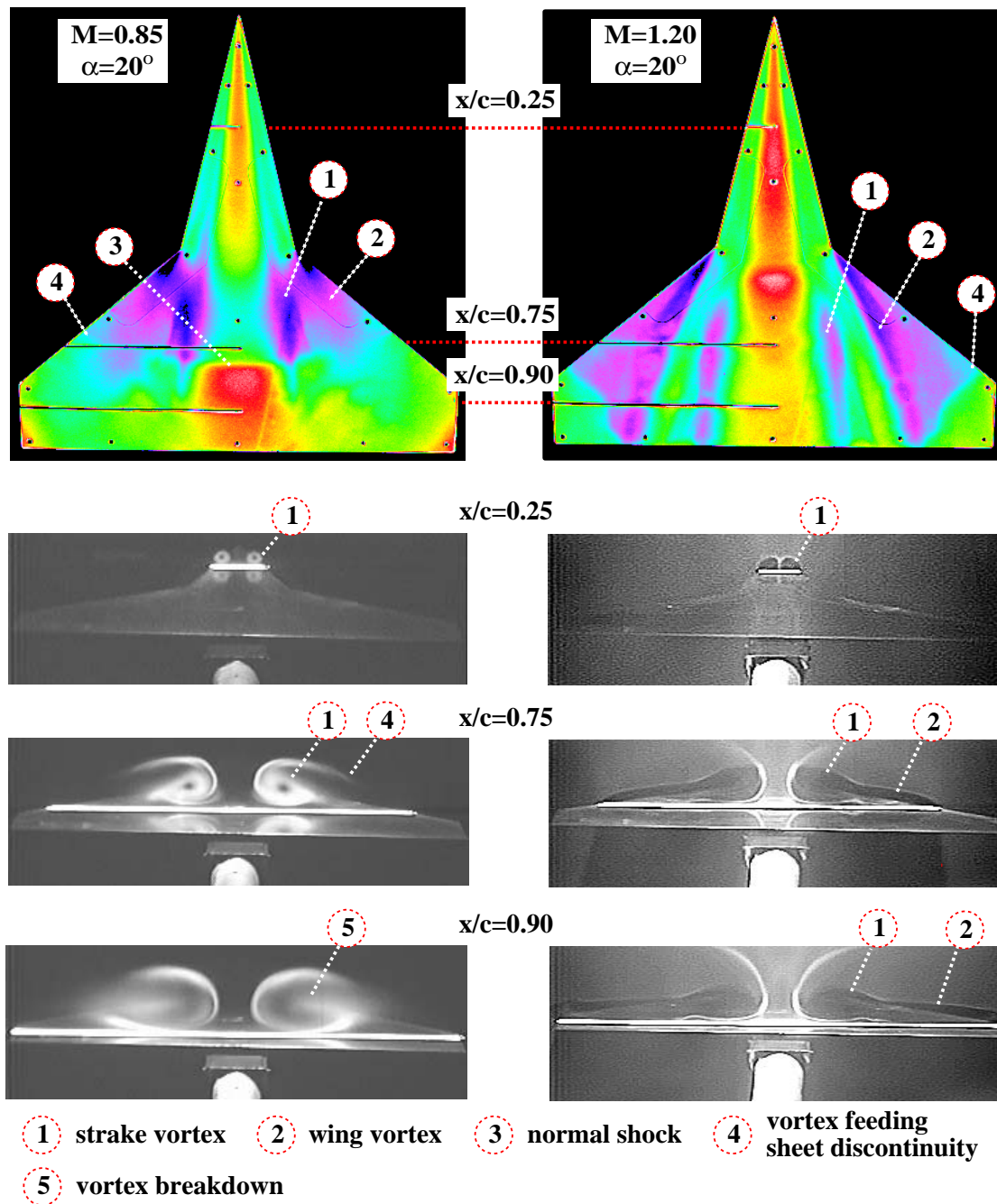


Fig. 12. Comparison of PSP and LVS images on the double delta wing model at $M = 0.85$ and $M = 1.20$, $\alpha = 20^\circ$

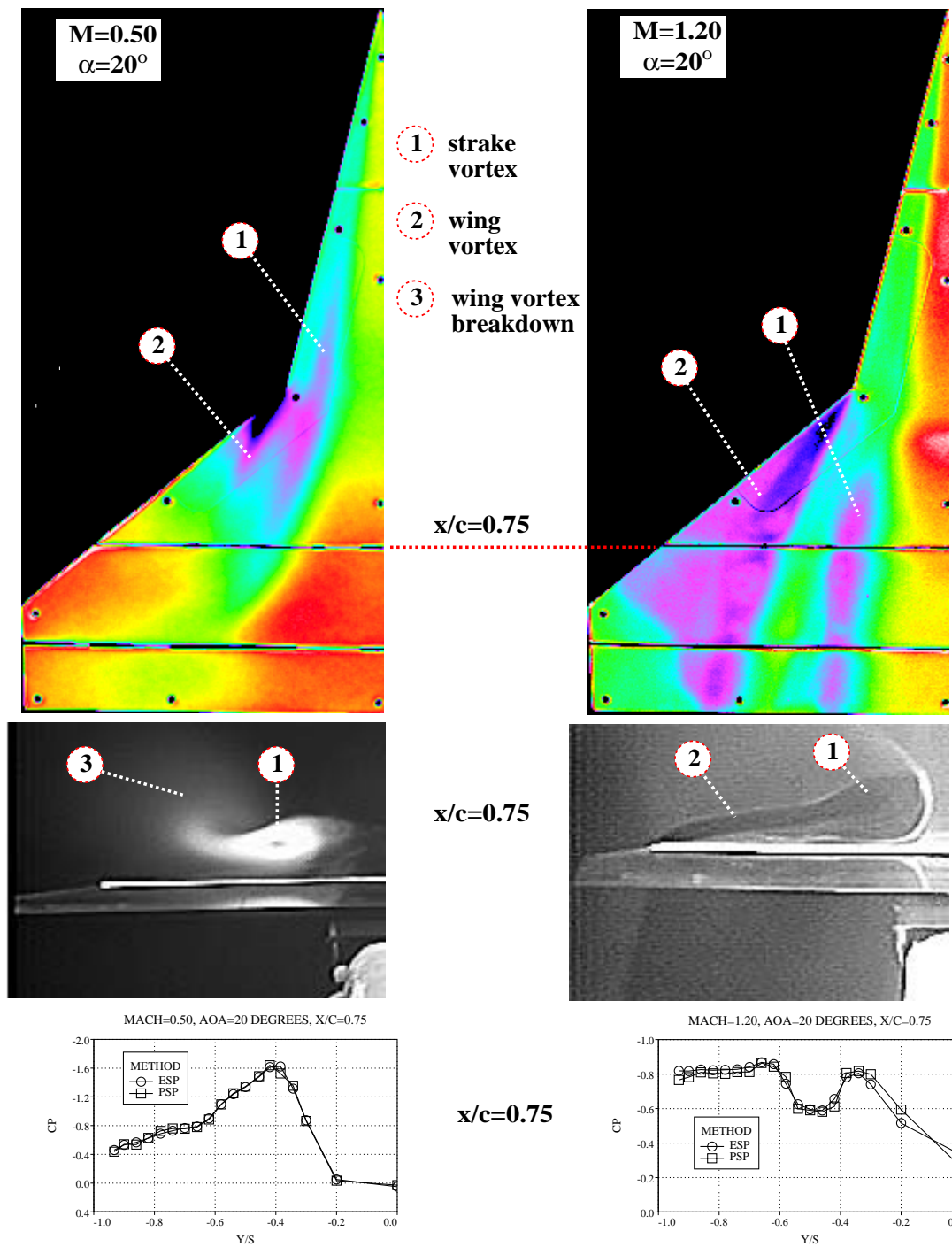


Fig. 13. Correlation of PSP and LVS images with spanwise pressure distributions on the double delta wing model at $M = 0.50$ and $M = 1.20$, $\alpha = 20^\circ$

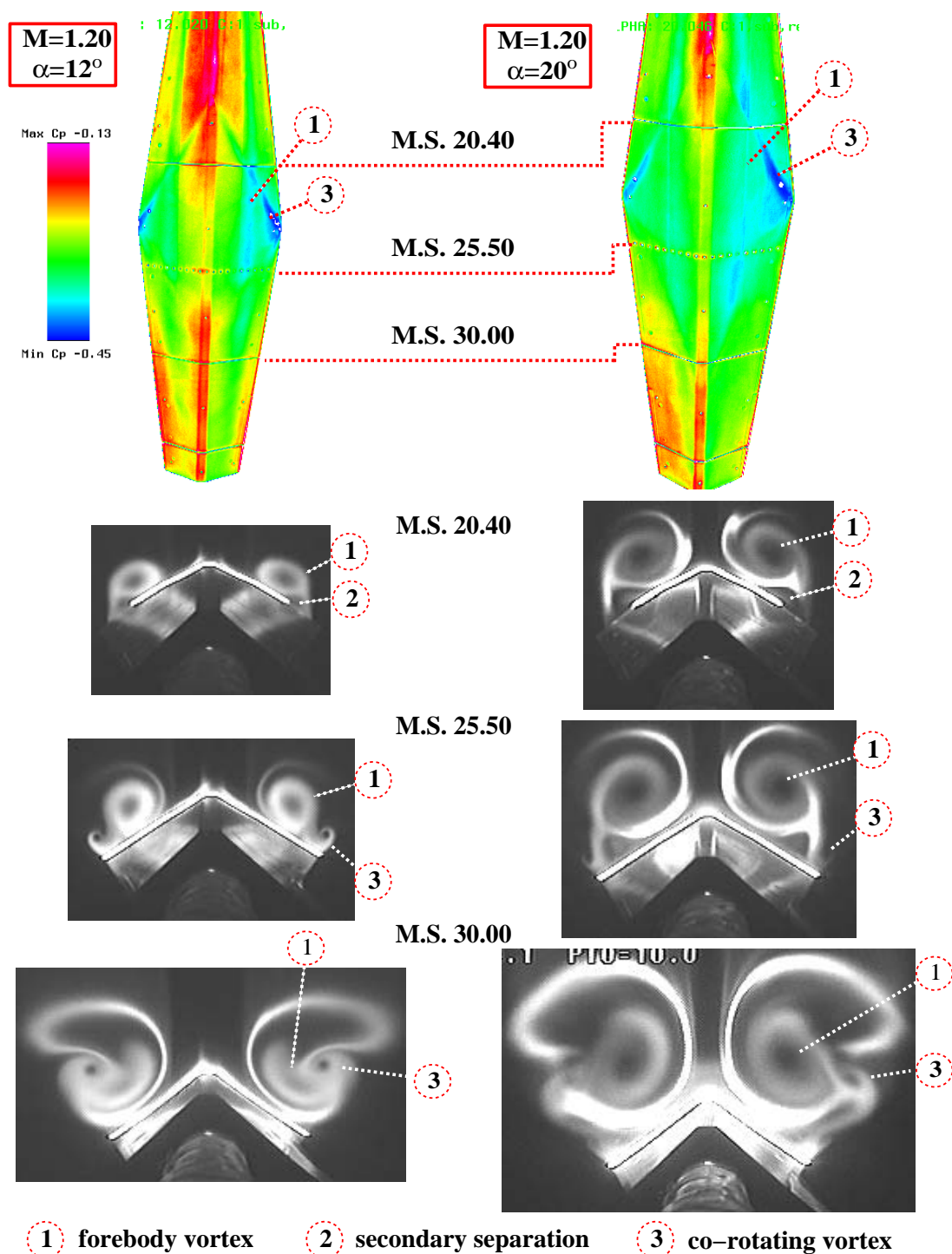


Fig. 14. Comparison of PSP and LVS images on the faceted missile model at $\alpha = 12^\circ$ and $\alpha = 20^\circ$, $M = 1.20$

UNIFIED APPLICATION OF VAPOR SCREEN FLOW VISUALIZATION AND PRESSURE SENSITIVE PAINT MEASUREMENT TECHNIQUES TO VORTEX- AND SHOCK WAVE-DOMINATED FLOW FIELDS

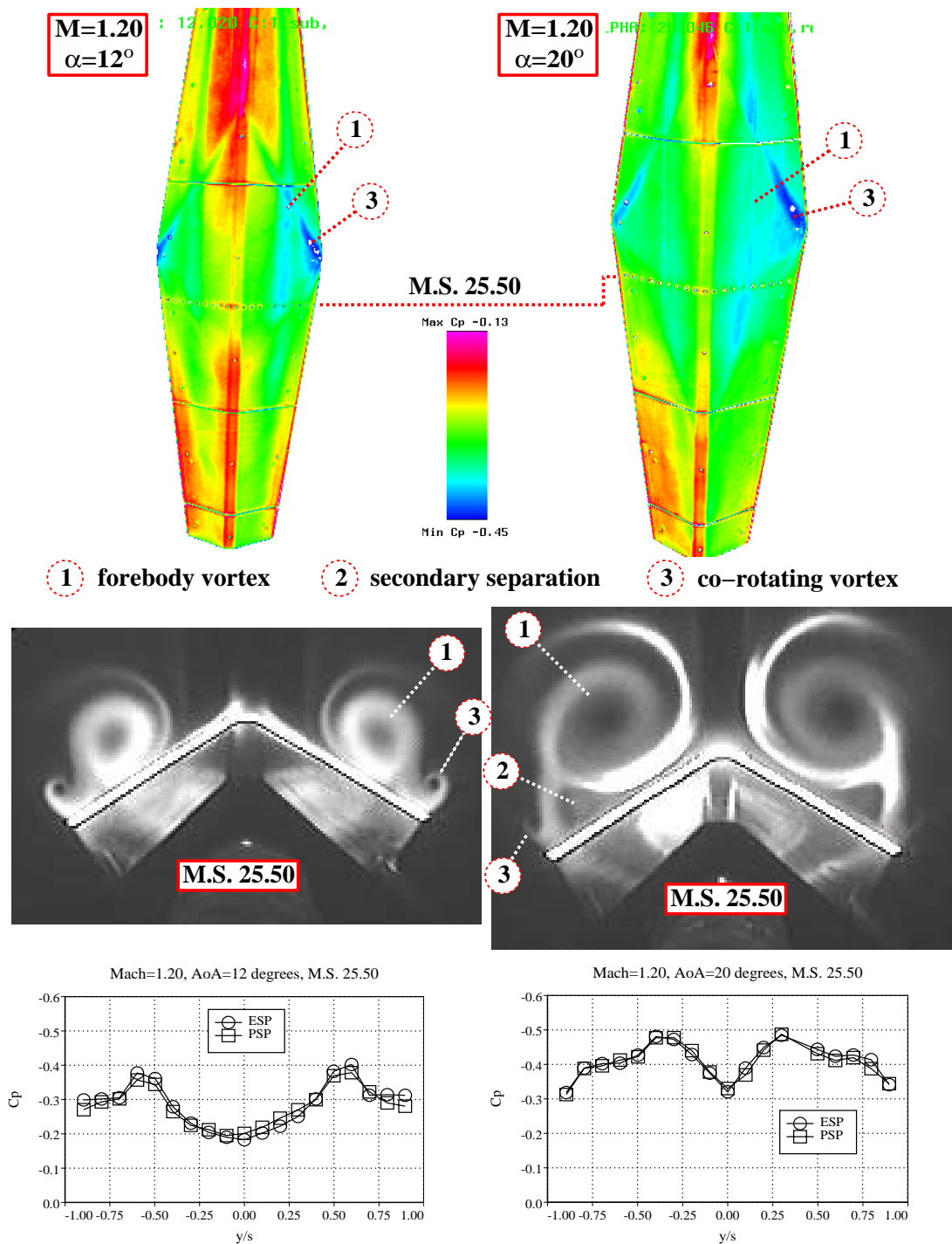


Fig. 15. Correlation of PSP and LVS images with spanwise pressure distributions on the faceted missile model at $\alpha = 12^\circ$ and $\alpha = 20^\circ$, $M = 1.20$

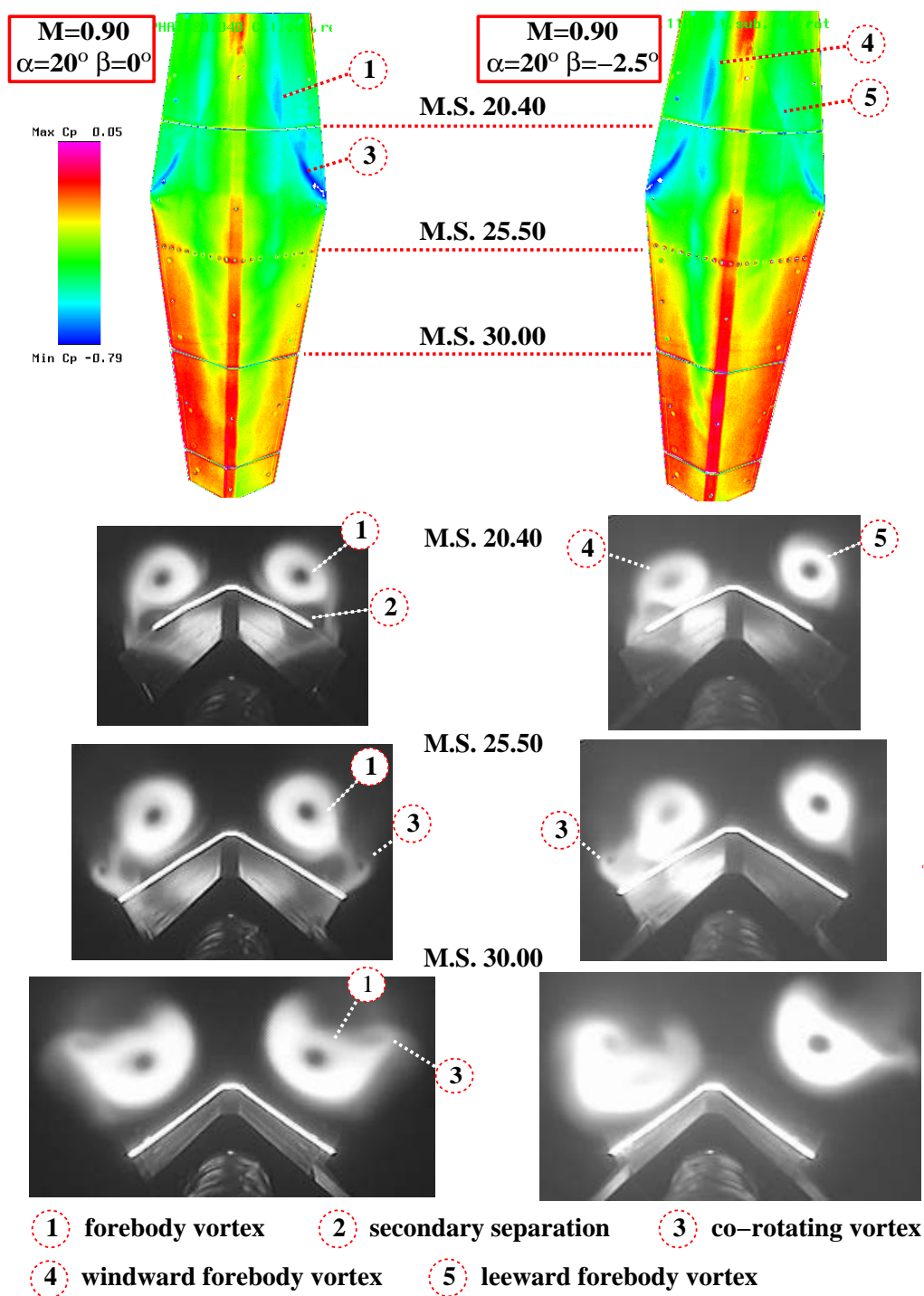


Fig. 16. Comparison of PSP and LVS images on the faceted missile model at $\beta = 0^\circ$ and $\beta = -2.5^\circ$, $M = 0.90$, $\alpha = 20^\circ$

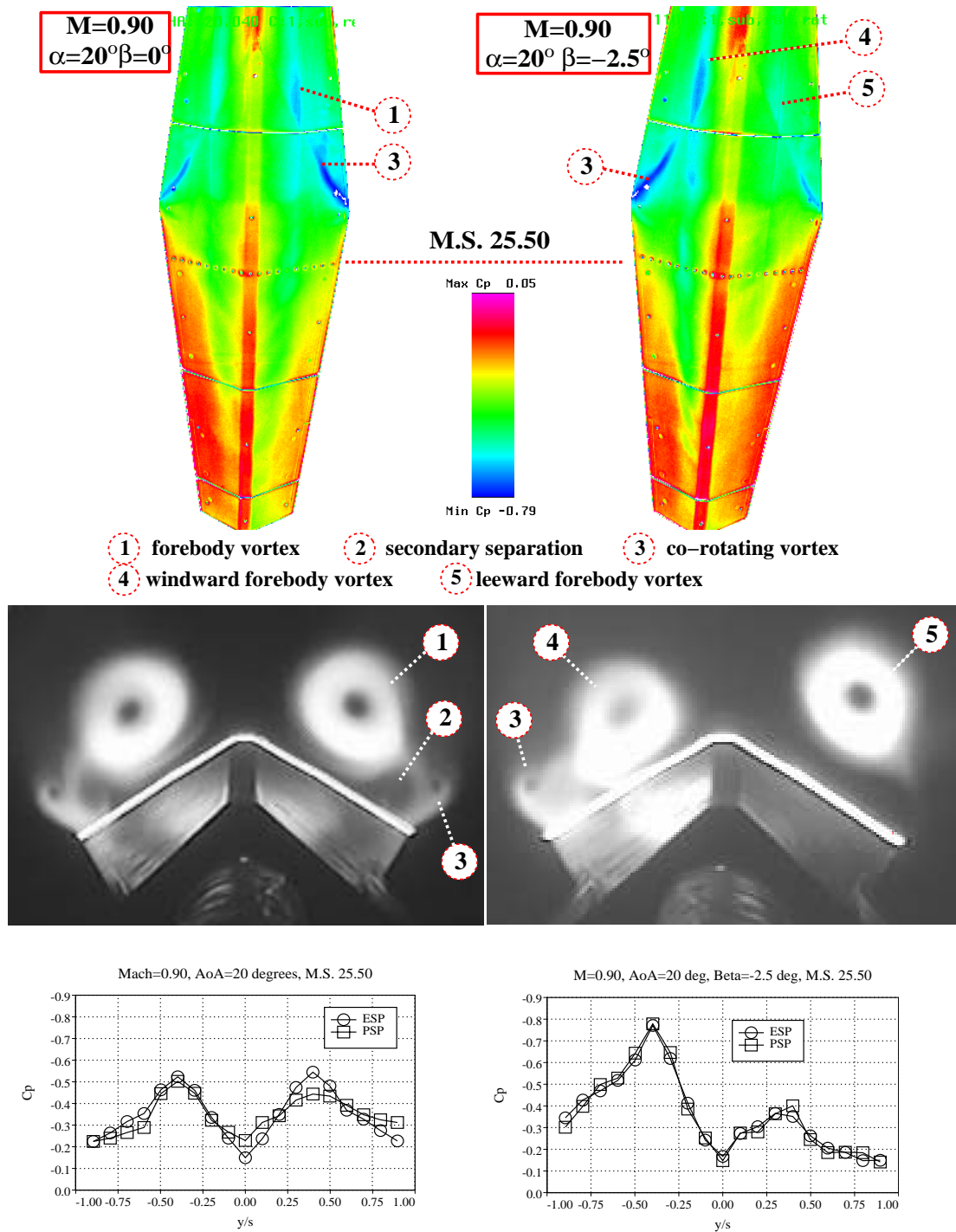


Fig. 17. Correlation of PSP and LVS images with spanwise pressure distributions on the faceted missile model at $\beta = 0^\circ$ and $\beta = -2.5^\circ$, $M = 0.90$, $\alpha = 20^\circ$